



Enhanced activity and sulfur resistance for soot combustion on three-dimensionally ordered macroporous-mesoporous $\text{Mn}_x\text{Ce}_{1-x}\text{O}_8/\text{SiO}_2$ catalysts

Xuehua Yu^a, Lanyi Wang^{a,b}, Maozhong Chen^a, Xiaoqiang Fan^a, Zhen Zhao^{a,b,*}, Kai Cheng^c, Yongsheng Chen^{c,**}, Zbigniew Sojka^d, Yuechang Wei^b, Jian Liu^b

^a Institute of Catalysis for Energy and Environment, College of Chemistry and Chemical Engineering, Shenyang Normal University, Shenyang, Liaoning, 110034, China

^b State Key Laboratory of Heavy Oil Processing, China University of Petroleum, 18# Fuxue Road, Chang Ping, Beijing 102249, China

^c Energy and Catalysis Laboratory, Department of Mechanical and Automation Engineering, The Chinese University of Hong Kong, Shatin, NT, Hong Kong, China

^d Faculty of Chemistry, Jagiellonian University, ul. Ingardena 3, 30-060 Kraków, Poland

ARTICLE INFO

Keywords:

Soot combustion

$\text{Mn}_x\text{Ce}_{1-x}\text{O}_8$

3DOM structure

Ordered mesoporous structure

Catalysts

ABSTRACT

A series of $\text{Mn}_x\text{Ce}_{1-x}\text{O}_8/3\text{DOM-m SiO}_2$ catalysts with different $\text{Mn}_{0.5}\text{Ce}_{0.5}\text{O}_8$ loadings and different x values were designed and successfully prepared by a very simple method. The as-prepared catalysts, which contain three-dimensionally ordered macroporous (3DOM) structure embedded with ordered mesoporous structure, exhibit high catalytic activity and good stability for soot combustion. The good catalytic performances of as-prepared catalysts are owing to facilitated soot transport through the macroporous structure and synergistic effect between Mn and Ce for the activation of gas molecules (NO and O_2) within the mesoporous structure. In addition, the sulfur and water tolerance of as-prepared catalysts were tested and the reasons for sulfur and water tolerance also well illustrated. The probable soot combustion mechanisms are proposed based on the characterization results and DFT calculation. More importantly, this work demonstrates the rational design and facile preparation of highly efficient catalysts for reactions between large solid particles and small gas molecules.

1. Introduction

In the past decades, diesel engines have been widely used in heavy-duty implements and light-duty trucks because of their higher thermal efficiency and lower fuel consumption than gasoline engines [1]. However, serious environmental problems are caused by diesel exhausts, especially particulate matter (PM) and nitrogen oxides (NO_x) [2]. Specifically, particulate matter emitted from diesel engines is harmful to human beings and other creatures, and it has become one of the reasons for hazy weather [3]. Thus, it is important to find ways to mitigate the emissions from diesel engines. Because PM and NO_x are favorably formed under different conditions, it is difficult to remove harmful diesel exhausts only by engine modification and clean oil technologies [4]. Thus, catalytic after-treatment devices are commonly used [5], and design and synthesis of novel catalysts with good catalytic activity and stability for soot combustion is one of the key issues for the purification of diesel exhausts [6].

As we all know, soot combustion involves typical $\text{gas}(\text{O}_2)\text{-solid}$

(soot)-solid(catalyst) heterogeneous catalysis and deep oxidation reaction, which takes place at the three-phase boundary [7]. Therefore, catalytic performance is affected by several factors including contact efficiency between the catalyst and the soot, intrinsic catalytic activity, and activation of gas molecules. Generally speaking, conventional catalysts with micro- and meso-pores ($< 10 \text{ nm}$) usually have high surface area and good catalytic performance for gas phase catalytic reactions [8]. However, it is very difficult for soot particles with diameter larger than 25 nm to enter the inner pores and access the internal active sites. To enhance the contact efficiency between the catalyst and the soot, novel catalysts with different morphologies, such as space-open array catalysts, three-dimensional and networked catalysts, fibrous catalysts, and three-dimensionally ordered macroporous (3DOM) catalysts, have been designed, synthesized, and reported in the literature [9,10]. Specifically, 3DOM catalysts with large pore sizes ($> 50 \text{ nm}$) and interconnected macroporous structure suffer less transport and diffusion resistance and provide sufficient space for migration of soot particles in their inner pores [11,12]. Recently, several kinds of 3DOM catalysts, for

* Corresponding author at: Institute of Catalysis for Energy and Environment, College of Chemistry and Chemical Engineering, Shenyang Normal University, Shenyang, Liaoning, 110034, China.

** Corresponding author at: Energy and Catalysis Laboratory, Department of Mechanical and Automation Engineering, The Chinese University of Hong Kong, Shatin, NT, Hong Kong, China.

E-mail addresses: zhenzhao@cup.edu.cn, zhaozhen1586@163.com (Z. Zhao), yschen@mae.cuhk.edu.hk (Y. Chen).

<https://doi.org/10.1016/j.apcatb.2019.04.097>

Received 6 July 2018; Received in revised form 28 April 2019; Accepted 29 April 2019

Available online 03 May 2019

0926-3373/ Crown Copyright © 2019 Published by Elsevier B.V. All rights reserved.

example, transition-metal oxides, alkaline metal oxides, perovskite-type oxides, and ceria-based catalysts, were prepared and applied for soot combustion. Those 3DOM catalysts exhibited high catalytic activity for soot combustion owing to the improved contact efficiency between the catalyst and the soot [13].

Most oxide-based 3DOM catalysts, however, possess low intrinsic catalytic activities at low temperatures, thus, efforts have been made to enhance their intrinsic activities. So far, Au, Pt, Pd, Ag, etc., have been used as active components in the catalysts for soot combustion owing to their activation ability for O₂ at low temperatures [14,15]. In our previous works, a series of 3DOM oxides-supported Au and Pt catalysts were prepared and they exhibited high catalytic activities for soot combustion [16–18]. However, due to the limited resources, the high costs of noble metal catalysts hinder their extensive applications. For this reason, a lot of low-cost catalysts have been also prepared and studied for soot combustion. Many previous studies demonstrated that CeO₂-based oxides are promising candidate catalysts for soot combustion owing to their oxygen storage/release capacity (OSC) [19,20]. Meanwhile, manganese oxides with variable valence states of Mn⁴⁺, Mn³⁺, or Mn²⁺ also exhibit high catalytic activities for soot combustion, especially for storage/release of NO_x [21,22]. MnO_x-CeO₂ mixed oxides with synergistic effect between Mn and Ce have been shown to have high intrinsic activity in soot combustion [23,24].

In addition, activation of gas molecules is also important for catalytic performance of the catalysts, there is, however, not much work in the literature focusing on this aspect [25,26]. As an oxidant, the gas molecules (especially O₂) play a decisive role in soot combustion. Therefore, the activation of gas molecules can significantly influence the catalytic performance of catalysts. As mentioned before, catalysts with nanometer-scale multi-pores or ordered mesoporous structures are favorable for the activation of gas molecules. [27,28] At present, design and preparation of novel catalysts with optimal combination of the three factors mentioned above, is still a big challenge, especially for metallic oxides with both ordered macroporous and mesoporous structures [29]. It has been shown that SiO₂ with 3DOM structure and ordered mesopores can be easily prepared through alkoxide based sol-gel processes [30,31]. Unlike metal oxides, the formed three-dimensionally ordered macroporous-mesoporous (3DOM-m) SiO₂ structures also exhibit strong mechanical stability when they act as catalysts or supports. Meanwhile, the costs for preparation of 3DOM-m SiO₂ are lower than that of metal oxides. For these reasons, Mn_xCe_{1-x}O₈/3DOM-m SiO₂ with 3DOM structure and ordered mesopores, in which Mn_xCe_{1-x}O₈ mixed oxides are nanoparticles and supported on 3DOM-m SiO₂, are prepared and expected to exhibit excellent catalytic performance for soot combustion.

In this work, a series of novel Mn_xCe_{1-x}O₈/3DOM-m SiO₂ catalysts, which contain 3DOM structure and ordered mesopores in the SiO₂, were prepared by simple incipient wetness impregnation method. 3DOM-m SiO₂ support was synthesized by colloidal crystal template (CCT) method and mesoporous structure was also formed in the process of CCT method. The as-prepared catalysts exhibit high catalytic activities for soot combustions owing to macroporous structure for soot transport, mesoporous structure for activation of gas molecules (NO, O₂), and synergistic effect between Mn and Ce. In addition, the influences of NO, stability and sulfur and water tolerance of as-prepared catalysts are also studied. The probable mechanisms for soot combustion are discussed based on the characterization results and DFT calculation.

2. Experimental section

2.1. Catalyst preparation

2.1.1. Synthesis of 3DOM-m SiO₂

3DOM-m SiO₂ was prepared by the colloidal crystal template (CCT) method, using PMMA arrays as macroporous template, P123 as

mesoporous template, and tetraethyl orthosilicate (TEOS) as precursors. The PMMA microspheres were synthesized by a modified emulsifier-free emulsion polymerization method, which was reported previously [32]. In a typical process, P123 was dissolved in a mixture of anhydrous alcohol, water, and HCl aqueous solution, and then TEOS was added dropwise. Afterwards, the solution was stirred in a water bath at 45 °C for 2 h and kept at 25 °C for 2 h. Then, the PMMA arrays were immersed in the solution until no bubbles emerged. After completely impregnated, the PMMA arrays were separated by vacuum filter and dried at 40 °C for 24 h. The final dried sample was calcined in a tube furnace under an air flow to remove the template. The temperature was ramped at 1 °C min⁻¹ from room temperature to 310 °C, and was kept at 310 °C for 3 h, followed by another temperature ramp from 310 °C to 600 °C at a rate of 1 °C min⁻¹ in an air flow. 3DOM-m SiO₂ support was obtained after it was kept at 600 °C for 3 h.

2.1.2. Synthesis of 3DOM-m SiO₂-supported Mn_xCe_{1-x}O₈ catalysts

3DOM-m SiO₂-supported Mn_xCe_{1-x}O₈ catalysts were synthesized by the incipient wetness impregnation method. In a typical process, proper amounts of Ce(NO₃)₃ and Mn(NO₃)₂ solids were dissolved in deionized water, and the volume of the solution was equal to the pore volume of the 3DOM-m SiO₂ support. Then, the impregnated 3DOM-m SiO₂ was dealt with ultrasound for 5 min and dried at 80 °C for 24 h. After that, the sample was calcined at 550 °C for 4 h in a tube furnace, and 3DOM-m SiO₂-supported Mn_xCe_{1-x}O₈ catalysts were obtained. Thus, by changing the amounts of Ce(NO₃)₃ and Mn(NO₃)₂ solids, 3DOM-m SiO₂-supported Mn_xCe_{1-x}O₈ catalysts with different molar ratios of Ce to Mn were obtained. In order to show the advantages of 3DOM-m structure, silica-supported Mn_{0.5}Ce_{0.5}O₈ was also synthesized using the same synthesis procedure. In addition, the synthesis steps of powder Mn_{0.5}Ce_{0.5}O₈ catalyst are listed in the supplementary information. The synthesis recipe of the catalysts is listed in the Table 1.

2.2. Physical and chemical characterization

XRD patterns were recorded on a powder X-ray diffractometer (Ultima IV, Rigaku) using Cu Kα radiation as the source with a Ni filter. Data were collected between 2θ = 10–80° with an increment of 0.02°. The patterns were compared with JCPDS reference data for phase identification. The field emission scanning electron microscopy (FESEM, Quanta 200 F) was used for characterization of catalyst surface morphology. Before FESEM testing, the samples were smeared on conducting resin and coated with 10 nm Au. TEM images were obtained using a JEOL JEM-2100 transmission electron microscope. Raman spectra of the samples were measured in the region of 200–1800 cm⁻¹ using a HORIBA LabRAM HR Evolution spectrometer. The Raman spectra were obtained with 532 nm and 325 nm lasers and a 50× long-focus lens. The time and power of acquisition were 10 s (50 s for UV-Raman) and 5 mW (1.5 mW for UV-Raman). The BET specific surface areas were calculated using the linear part of the BET plot of the N₂ isotherms and mesoporous distribution curve performed on a Micromeritics TriStar II: 3020 analyzer. X-ray photoelectron spectra (XPS) were recorded on a Thermo ESCALAB 250Xi. The binding energies were calibrated by setting C1s peak of adventitious carbon at 284.6 eV.

H₂-TPR measurements were performed using a TP-5076 adsorption instrument, Tianjin, China. A sample of 100 mg was placed in a fixed-bed tubular quartz reactor and pre-treated in flowing N₂ at 300 °C for 1 h. After cooling to 40 °C, the gas flow was switched to 50 ml min⁻¹ 10-vol% H₂/N₂ and the temperature ramped to 880 °C at a rate of 10 °C min⁻¹. The consumption of hydrogen was recorded by a thermal conductivity detector (TCD). O₂-temperature programmed desorption (TPD) measurements were also carried on the same instrument. A sample of 100 mg was placed in a fixed-bed tubular quartz reactor and pre-treated in Air at 300 °C for 1 h. After cooling to 40 °C, the flow gas was switched to 50 ml min⁻¹ He and the temperature ramped to 800 °C

Table 1Recipe for the synthesis of $\text{Mn}_x\text{Ce}_{1-x}\text{O}_8/3\text{DOM-m SiO}_2$ catalysts with different $\text{Mn}_{0.5}\text{Ce}_{0.5}\text{O}_8$ loadings and different Ce to Mn molar ratios.

Catalysts	Ce(NO ₃) ₃ /g	^a Mn(NO ₃) ₂ /g	3DOM-m SiO ₂ /g
CeO ₂ /3DOM-m SiO ₂	1.50	0	0.5
Mn _{0.2} Ce _{0.8} O ₈ /3DOM-m SiO ₂	1.20	0.24	0.5
Mn _{0.4} Ce _{0.6} O ₈ /3DOM-m SiO ₂	0.90	0.49	0.5
Mn _{0.6} Ce _{0.4} O ₈ /3DOM-m SiO ₂	0.60	0.74	0.5
Mn _{0.8} Ce _{0.2} O ₈ /3DOM-m SiO ₂	0.30	0.99	0.5
MnO ₈ /3DOM-m SiO ₂	0	1.23	0.5
10% Mn _{0.5} Ce _{0.5} O ₈ /3DOM-m SiO ₂	0.25	0.21	0.5
20% Mn _{0.5} Ce _{0.5} O ₈ /3DOM-m SiO ₂	0.50	0.41	0.5
30% Mn _{0.5} Ce _{0.5} O ₈ /3DOM-m SiO ₂	0.75	0.62	0.5
40% Mn _{0.5} Ce _{0.5} O ₈ /3DOM-m SiO ₂	1.00	0.82	0.5
50% Mn _{0.5} Ce _{0.5} O ₈ /3DOM-m SiO ₂	1.25	1.03	0.5
60% Mn _{0.5} Ce _{0.5} O ₈ /3DOM-m SiO ₂	1.50	1.23	0.5
80% Mn _{0.5} Ce _{0.5} O ₈ /3DOM-m SiO ₂	2.00	1.65	0.5
40% Mn _{0.5} Ce _{0.5} O ₈ /3DOM SiO ₂	1.00	0.82	0.5
^b 40% Mn _{0.5} Ce _{0.5} O ₈ /silica gel	1.00	0.82	0.5
Powder Mn _{0.5} Ce _{0.5} O ₈	1.00	0.82	2mL (25% ammonia)

^a : Mn(NO₃)₂ used in the experiments were 50 wt% Mn(NO₃)₂.^b: Silica gel was purchased from Damao Chemical Reagent Factory of Tianjin.

at a rate of 10 °C min⁻¹. The desorption of oxygen was recorded by the TCD.

In this work, the Vienna ab-initio simulation package (VASP) was used to calculate all states with the electron exchange correlation effect described by the Perdew-Burke-Ernzerhof functional within the generalized gradient approximation (GGA-PBE) [33]. The spin-polarized calculations were performed. PAW pseudopotential was used to describe the core-valence electron interaction. Plane-wave basis set with a cutoff energy of 400 eV was used in this work. A correction of Hubbard U term was added to the PBE functional (DFT + U) employing the rotationally invariant formalism. We set $U_{\text{eff,Ce}} = 4.5$ eV for the Ce 4f orbital and $U_{\text{eff,Mn}} = 4.5$ eV for the Mn 3d orbital [34]. Theoretical calculations predict that the CeO₂ (111) surface has a lower surface energy than the (110) and (100) planes [35]. So we built a periodic slab with four layers for cerium oxide (111) facets, i.e., 4 × 4 surface unit cells were used. We fixed the bottom two layers of cerium oxide. The vacuum gap thickness was set to 15 Å. Gaussian smearing was adopted with the width of the smearing of 0.05 eV. A Monkhorst pack 1 × 1 × 1 k-point mesh was used for the Brillouin zone integration.

During structural optimizations, all atoms except those in the bottom two layers of the slab were allowed to relax until atom forces were smaller than 0.05 eV/Å. Adsorption energy were calculated using the following expression:

$$E_{\text{ad}} = E_{\text{tot}} - E_{\text{slab}} - E_{\text{x}},$$

where E_{tot} is the total energy of the combined system with the adsorbate X bound to the slab, E_{slab} , the energy of the slab alone, and E_{x} , the energy of the adsorbate in the gas phase. According to this definition, exothermic adsorption results in a negative value of E_{ad} . The oxygen vacancy formation energy was calculated by $E_{\text{vac}} = E_{\text{de}} + 1/2E_{\text{O}_2} - E_{\text{slab}}$, where E_{de} is the energy of defective surface and E_{O_2} , the energy of a gas-phase O₂ molecule. The oxidation states of Ce atoms and Mn atoms determine their spin magnetic moments. For Ce⁴⁺, the spin magnetic moment is 0 μB; if one electron is transferred to Ce⁴⁺, it will occupy a 4f orbital and the spin magnetic moment change to 1 μB. For Mn⁴⁺ and Mn³⁺, the spin magnetic moments are within the range of 2.74–3.24 μB and 3.56–3.92 μB, respectively.

2.3. Activity measurements

The catalytic oxidation activities of as-prepared samples were evaluated with a temperature-programmed oxidation reaction (TPO) on a fixed-bed tubular quartz reactor ($\Phi = 8$ mm), and each TPO varied from 100 to 600 °C at a rate of 2 °C min⁻¹. The model soot was Printex-U particulates (25-nm diameter, Degussa). Elemental analysis of the

Printex-U particulates gave its composition as 92.0% C, 0.7% H, 3.5% O, 0.1% N, 0.2% S, and 3.5% others [18]. 100 mg catalyst and 10 mg soot were mixed by a spatula and their loose mixture was placed in the fixed-bed tubular quartz reactor. The oxidation reaction was carried out with a mixture gas containing 10% O₂ and 0.2% NO balanced with Ar at a flow rate of 50 mL min⁻¹. The outlet gas compositions were analyzed by an on-line gas chromatograph (GC, Agilent 7890B) equipped with a flame ionization detector (FID). Before entering the FID detector, CO and CO₂ were fully converted to CH₄ by a Ni catalyst maintained at 380 °C. The catalytic activity was evaluated using the values of T₁₀, T₅₀ and T₉₀, which were defined as the temperatures for 10%, 50%, and 90% soot conversions, respectively. The selectivity to CO₂ formation (S_{CO_2}) was defined as that the CO₂ outlet concentration (C_{CO_2}) divided by the sum of the CO₂ and CO outlet concentrations, i.e., $S_{\text{CO}_2} = C_{\text{CO}_2} / (C_{\text{CO}} + C_{\text{CO}_2})$. $S_{\text{CO}_2}^m$ was denoted as S_{CO_2} at the temperature (T_m) corresponding to the highest soot-burnt rate. The catalytic performance of the catalysts under different NO and SO₂ concentrations were tested by the same conditions except for the compositions of reaction mixture gases. In addition, the catalytic performance of the catalysts with the presence of water vapor were also investigated by the continuous bubble method, and the composition of reaction gas was 10% O₂, 10% H₂O, 0.2% NO, with/without SO₂ (100 or 300 ppm), and balanced with Ar at a flow rate of 50 mL min⁻¹. In order to investigate the stability of as-prepared catalysts, the catalytic performance of a catalyst after presulfurization and hydrothermal treatment was also measured and the treatment conditions are described in the supplementary information.

3. Results and discussion

3.1. Structural features of as-prepared catalysts

3.1.1. Textural properties of as-prepared catalysts

The textural properties of the 3DOM-m SiO₂ and 40% Mn_{0.5}Ce_{0.5}O₈/3DOM-m SiO₂ catalyst are shown in Fig. 1. The SEM image of 3DOM-m SiO₂ (Fig. 1a) shows it has well-aligned macropores with an average diameter of about 330 nm. This observation indicates that shrinkage of CCT templates happened in the heat treatment. In addition, the voids with diameter of 110 nm, which are interconnected through open windows. Fig. 1b exhibits the TEM image of 3DOM-m SiO₂. It can be seen that the walls of macropores are filled with ordered mesoporous structure. The arrangement of the mesoporous structure, which gives curved line patterns parallel to the macropore wall and honeycomb arrays in the octahedral centers, was confirmed to be 2D hexagonal. Fig. 1c and d exhibit the nitrogen adsorption/desorption isotherm and

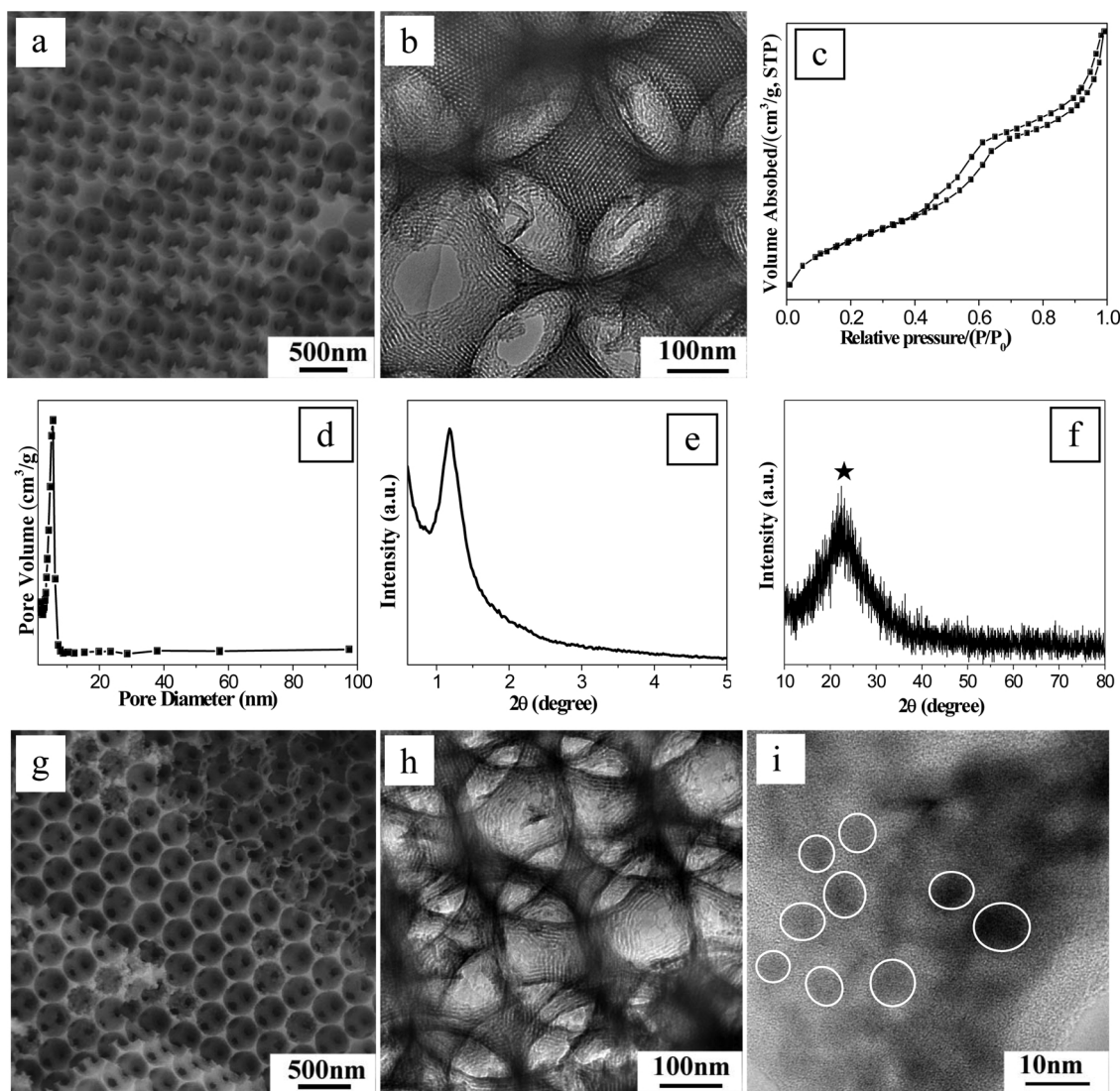


Fig. 1. Physical properties of as-prepared catalyst.

(3DOM-m SiO₂: a: SEM image; b: TEM image; c: N₂ adsorption-desorption isotherm; d: Pore distribution; e: Low angle X-ray diffraction pattern; f: X-ray diffraction pattern; 40% Mn_{0.5}Ce_{0.5}O_x/3DOM-m SiO₂: g: SEM image; h and i: TEM images).

Table 2

Textural properties of as-prepared catalysts.

Catalysts	Surface area(m ² /g) ^a	Total pore volume(cm ³ /g) ^b	Pore size(nm) ^c
3DOM-m SiO ₂	470.9	0.634	5.3
10%Ce _{0.5} Mn _{0.5} O _x /3DOM-m SiO ₂	295.2	0.380	5.1
20% Ce _{0.5} Mn _{0.5} O _x /3DOM-m SiO ₂	194.1	0.289	5.9
30% Ce _{0.5} Mn _{0.5} O _x /3DOM-m SiO ₂	197.2	0.277	5.6
40% Ce _{0.5} Mn _{0.5} O _x /3DOM-m SiO ₂	199.9	0.273	5.2
50% Ce _{0.5} Mn _{0.5} O _x /3DOM-m SiO ₂	175.6	0.276	6.2
60% Ce _{0.5} Mn _{0.5} O _x /3DOM-m SiO ₂	160.6	0.280	6.9
80% Ce _{0.5} Mn _{0.5} O _x /3DOM-m SiO ₂	147.6	0.264	7.1
CeO ₂ /3DOM-m SiO ₂	170.6	0.317	7.4
Mn _{0.2} Ce _{0.8} O _x /3DOM-m SiO ₂	169.4	0.282	6.6
Mn _{0.4} Ce _{0.6} O _x /3DOM-m SiO ₂	178.5	0.279	6.2
Mn _{0.6} Ce _{0.4} O _x /3DOM-m SiO ₂	201.8	0.280	5.5
Mn _{0.8} Ce _{0.2} O _x /3DOM-m SiO ₂	206.9	0.269	5.2
MnO _x /3DOM-m SiO ₂	249.8	0.321	5.2

a: Calculated by BET method; b: Calculated by BJH desorption cumulative volume of pores between 1.7 nm and 300 nm diameter; c: Calculated by BJH desorption average pore diameter.

pore size distribution of the 3DOM-m SiO₂. A typical reversible type-IV adsorption isotherm is present and the pore size distribution of mesopores has a range of 2–8 nm. Fig. 1d illustrates that the mesopore size distribution of 3DOM-m SiO₂ is narrow. As shown in Table 2, the BET surface area of the 3DOM-m SiO₂ is 470.9 m²/g and the average pore diameter, 5.3 nm. To probe the orderliness of the mesopores, the low angle X-ray diffraction pattern of 3DOM-m SiO₂ is shown in Fig. 1e. An obvious diffraction peak at $2\theta = 0.9\text{--}1.5^\circ$ manifesting highly ordered mesostructures in the 3DOM-m SiO₂. Fig. 1f exhibits wide-angle X-ray diffraction pattern of the 3DOM-m SiO₂. There is a broad diffraction peak at 2θ of 22.5° (marked with “★”), which is typical for amorphous silica. The above results show that amorphous silica with three-dimensionally ordered macroporous and mesoporous structures was successfully synthesized. Fig. 1g shows well-aligned macropores, indicating that the 3DOM structure of 3DOM-m SiO₂ is preserved in the synthesis process. Fig. 1h illustrates that the ordered mesopores well remain after the loading process. Due to the confinement effect of mesopores, the Mn_xCe_{1-x}O₈ composite oxides form small nanoparticles and the diameters of the nanoparticles are smaller than 8 nm, which are marked with circles in Fig. 1i. For comparison, the SEM and TEM images of powder Mn_{0.5}Ce_{0.5}O₈ and 40% Mn_{0.5}Ce_{0.5}O₈/silica gel are also shown in Figures S1a–d. Without confinement, the diameters of the Mn_xCe_{1-x}O₈ particles are larger than 30 nm.

3.1.2. XRD results of as-prepared catalysts

The XRD patterns of the Mn_xCe_{1-x}O₈/3DOM-m SiO₂ catalysts with different Mn_{0.5}Ce_{0.5}O₈ loadings and different Ce to Mn molar ratios are shown in Fig. 2. The peaks at 2θ of 28.7° (111), 33.3° (200), 47.7° (220), and 56.5° (311) correspond to cerianite of CeO₂ (marked with “△” in Fig. 2A). Small shift in diffraction peaks in higher angles is observed

when compared with the standard cerianite of pure CeO₂ (PDF#43-1002). In addition, the intensities of the characteristic peaks increase with the Mn_{0.5}Ce_{0.5}O₈ loading, and the typical peak of amorphous silica (marked with “★” in Fig. 1f) gradually disappears. It suggests that Mn_{0.5}Ce_{0.5}O₈ composite oxides are supported on the skeleton surface of 3DOM-m SiO₂. Fig. 2B exhibits the XRD patterns of the Mn_xCe_{1-x}O₈/3DOM-m SiO₂ catalysts with different Ce to Mn molar ratios. Compared with CeO₂/M-m SiO₂ (Fig. 2Ba), the characteristic peaks of the Mn_xCe_{1-x}O₈/3DOM-m SiO₂ catalysts exhibit those of CeO₂ when the x value is less than 0.8 (marked with “△” in Fig. 2B). In addition, a slight peak shift is observed from 28.5° to 28.7° (the insert of Fig. 2B). The characteristic peaks of CeO₂ and their shift in the Mn_xCe_{1-x}O₈/3DOM-m SiO₂ catalysts (the x value is less than 0.8) indicate that Mn ions have been doped into the crystal lattice of CeO₂ owing to the smaller ionic radii of Mn⁴⁺ (0.054 nm), Mn³⁺ (0.066 nm), and Mn²⁺ (0.080 nm) than those of Ce⁴⁺ (0.094 nm) and Ce³⁺ (0.114 nm) [36]. When the x value is 0.8, no diffraction patterns are observed. The results are in good agreement with the recent report concerning the structural features of MnO_x-CeO₂ composite oxides. [37] As shown in Fig. 2Bf, the peaks for the MnO₈/3DOM-m SiO₂ catalyst are at 2θ of 23.1° (211), 32.9° (222), 38.2° (400), and 55.2° (044) belonging to bixbyite Mn₂O₃ (marked with “▲” in Fig. 2B, PDF#41-1442). Besides the bixbyite Mn₂O₃, the MnO₈/3DOM-m SiO₂ catalyst also exhibits other diffraction peaks, which may be from Mn₃O₄ (marked with “●” in Fig. 2B, PDF#18-0803).

3.1.3. N₂ Adsorption-desorption results of as-prepared catalysts

To investigate the pore properties of as-prepared catalysts, N₂ adsorption-desorption isotherms were collected and the results are shown in Figure S2. All Mn_{0.5}Ce_{0.5}O₈/3DOM-m SiO₂ catalysts with different Mn_{0.5}Ce_{0.5}O₈ loadings exhibit type IV adsorption isotherms (Figure S2A). However, two kinds of hysteresis loops are observed in the relative pressure (p/p_0) ranges of 0.8–1.0 and 0.4–0.8 in Figure S2A. The hysteresis loops in the higher pressure range (0.8–1.0) are of type H2. The size of the H2 hysteresis loop increases with the Mn_{0.5}Ce_{0.5}O₈ loading. The hysteresis loops in the lower pressure range (0.4–0.8) have characteristic of H1 hysteresis loop and the pore size decreases with the Mn_{0.5}Ce_{0.5}O₈ loading. From Figure S2B, it can be observed that Mn_xCe_{1-x}O₈/3DOM-m SiO₂ catalysts with different Mn to Ce molar ratios also exhibit type IV adsorption isotherms. Two kinds of hysteresis loops are present of type H2 hysteresis loop in p/p_0 range of 0.8–1.0 and of H1 hysteresis loop in p/p_0 range of 0.4–0.8. With increasing x value, the size of type H2 hysteresis loop in the higher p/p_0 range of 0.8–1.0 decreases while that of type H1 hysteresis loop increases in the lower p/p_0 range of 0.4–0.8. These two kinds of hysteresis loops suggest that two types of pore structures co-exist in as-prepared catalysts.

In order to further probe the types of pore structure and the influence of Mn_xCe_{1-x}O₈ on the pore structure of 3DOM-m SiO₂, the pore size distributions of as-prepared catalysts were tested and the results are shown in Fig. 3. As shown in Fig. 3A, the mesopore diameters of the Mn_xCe_{1-x}O₈/3DOM-m SiO₂ catalysts with different Mn_{0.5}Ce_{0.5}O₈ loadings are between 2 and 8 nm, and the presence of the Mn_{0.5}Ce_{0.5}O₈ nanoparticles has no significant effect on the mesopore size of the 3DOM-m SiO₂. Meanwhile, the pore volume decreases with the Mn_{0.5}Ce_{0.5}O₈ loading. In addition, mesoporous structures with diameter of 10–40 nm appear, and the intensity of mesoporous structure increases with the Mn_{0.5}Ce_{0.5}O₈ loading. Those mesoporous structures with diameter of 10–40 nm are attributed to the pores of the Mn_{0.5}Ce_{0.5}O₈ nanoparticles. In Fig. 3B, the Mn_xCe_{1-x}O₈/3DOM-m SiO₂ catalysts with different Mn and Ce compositions exhibit the same mesoporous structure with pore diameters smaller than 8 nm. In addition, another mesoporous structure with the diameters of 10–40 nm is present when the x value is less than 0.6, and the pore volume of these mesopores decreases with the x value. In other words, the pore volume increases with the Ce content in the Mn_xCe_{1-x}O₈/3DOM-m SiO₂

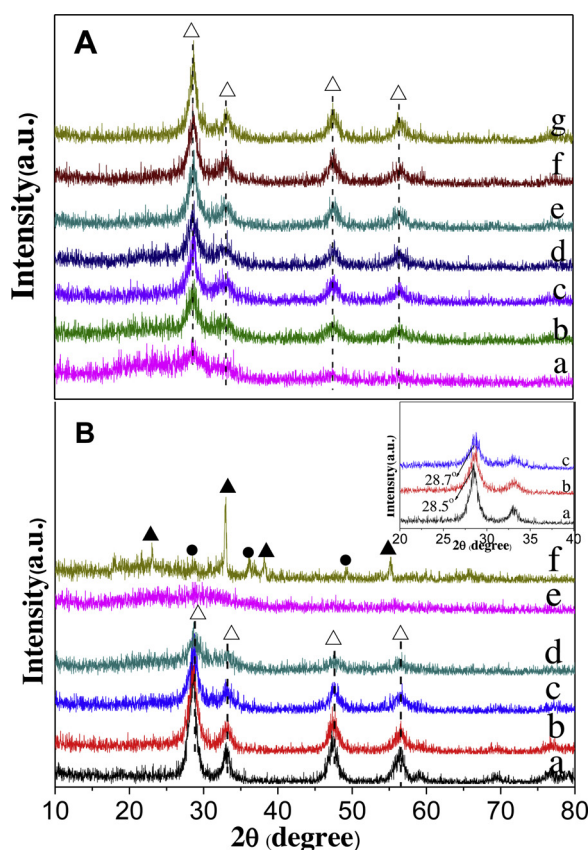


Fig. 2. X-ray diffraction patterns of the Mn_xCe_{1-x}O₈/3DOM-m SiO₂ catalysts with different Mn_{0.5}Ce_{0.5}O₈ loadings (A) and x values (B). (A: a: 10%; b: 20%; c: 30%; d: 40%; e: 50%; f: 60%; g: 80%; B: a: x = 0; b: x = 0.2; c: x = 0.4; d: x = 0.6; e: x = 0.8; f: x = 1).

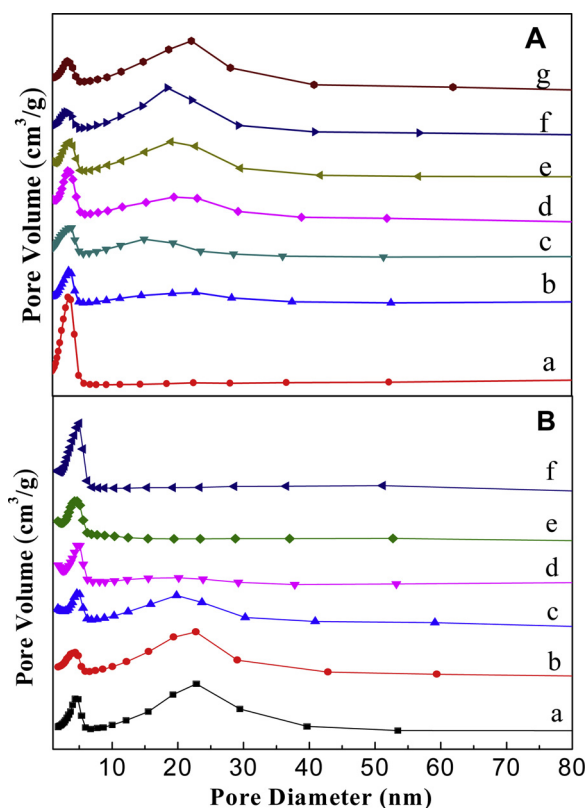


Fig. 3. Pore size distributions in the $\text{Mn}_x\text{Ce}_{1-x}\text{O}_8/\text{3DOM-m SiO}_2$ catalysts with different $\text{Mn}_{0.5}\text{Ce}_{0.5}\text{O}_8$ loadings (A) and x values (B).

(A: a: 10%; b: 20%; c: 30%; d: 40%; e: 50%; f: 60%; g: 80%; B: a: $x = 0$; b: $x = 0.2$; c: $x = 0.4$; d: $x = 0.6$; e: $x = 0.8$; f: $x = 1$).

catalysts, thus, it is inferred that these mesopores are attributed to the CeO_2 nanoparticles.

Table 2 lists the textural properties of as-prepared catalysts. The bare 3DOM-m SiO_2 exhibits largest surface area among as-prepared catalysts, and the value reaches $470.9 \text{ m}^2/\text{g}$. When the $\text{Mn}_x\text{Ce}_{1-x}\text{O}_8$ composite oxides are loaded on the 3DOM-m SiO_2 , the surface area of catalysts drastically decreases. With the increasing of $\text{Mn}_{0.5}\text{Ce}_{0.5}\text{O}_8$ loading, the surface area of the $\text{Mn}_{0.5}\text{Ce}_{0.5}\text{O}_8/\text{3DOM-m SiO}_2$ catalysts decreases. The reason behind this trend is probably that most 3DOM-m SiO_2 surface is covered by the $\text{Mn}_{0.5}\text{Ce}_{0.5}\text{O}_8$ composite oxides when the $\text{Mn}_{0.5}\text{Ce}_{0.5}\text{O}_8$ loading reaches a certain value. Meanwhile, after incipient wetness impregnation, most mesoporous structures are also blocked by small $\text{Mn}_{0.5}\text{Ce}_{0.5}\text{O}_8$ composite oxides in the mesopores of 3DOM-m SiO_2 . In addition, the $\text{Mn}_{0.5}\text{Ce}_{0.5}\text{O}_8$ loading has less impact on the total pore volume and the pore size. The total pore volume is about $0.27\text{--}0.38 \text{ cm}^3/\text{g}$ and the pore size increases only from 5.1 nm to 7.1 nm. Table 2 shows that the surface area of $\text{Mn}_x\text{Ce}_{1-x}\text{O}_8/\text{3DOM-m SiO}_2$ catalysts varies with different Mn and Ce compositions. As a whole, the surface area increases with the manganese content. Considering the pore size distributions, the difference in surface area can be attributed to the deposition of $\text{Mn}_x\text{Ce}_{1-x}\text{O}_8$ composite oxides. Meanwhile, the pore sizes of $\text{Mn}_x\text{Ce}_{1-x}\text{O}_8/\text{3DOM-m SiO}_2$ catalysts also slightly increase with the cerium content.

3.1.4. H_2 -TPR and O_2 -TPD results of as-prepared catalysts

In order to investigate the relationship between catalytic activities and intrinsic redox properties, the reducibility of the catalysts was tested by H_2 -TPR measurements and the results are presented in Fig. 4. No reduction is obtained for the 3DOM-m SiO_2 , suggesting no redox property for the 3DOM-m SiO_2 as shown in Fig. 4Aa. Thus, it is speculated that the 3DOM-m SiO_2 has low catalytic activities for soot

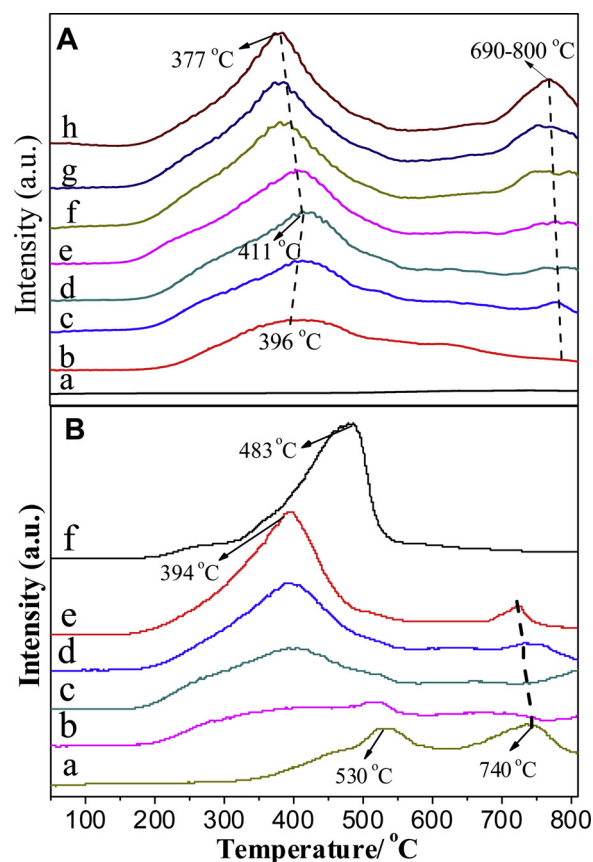


Fig. 4. H_2 -TPR profiles of the $\text{Mn}_x\text{Ce}_{1-x}\text{O}_8/\text{3DOM-m SiO}_2$ catalysts with different $\text{Mn}_{0.5}\text{Ce}_{0.5}\text{O}_8$ loadings (A) and x values (B).

(A: a: 0%; b: 10%; c: 20%; d: 30%; e: 40%; f: 50%; g: 60%; h: 80%; B: a: $x = 0$; b: $x = 0.2$; c: $x = 0.4$; d: $x = 0.6$; e: $x = 0.8$; f: $x = 1$).

combustion. In Fig. 4Aa-h, it can be seen that the reduction features of the $\text{Mn}_{0.5}\text{Ce}_{0.5}\text{O}_8/\text{3DOM-m SiO}_2$ catalysts with different $\text{Mn}_{0.5}\text{Ce}_{0.5}\text{O}_8$ loadings are similar. Two main reduction peaks appear in the ranges of $200\text{--}550^\circ\text{C}$ and $690\text{--}800^\circ\text{C}$. The first reduction peak in the temperature range of $200\text{--}550^\circ\text{C}$ is asymmetrical. It has been demonstrated that Mn oxides can be reduced and MnO is the final state in H_2 atmosphere, and this peak at $200\text{--}550^\circ\text{C}$ is assigned to the reduction of high valence states of Mn oxides (Mn^{n+} , $n > 2$) to MnO [32]. The asymmetrical peak suggests that there may be more than one reduction process in the temperature range of $200\text{--}550^\circ\text{C}$, namely, Mn^{4+} and Mn^{3+} may co-exist in the as-prepared catalysts and can be reduced to Mn^{2+} below 550°C . Besides the reduction of Mn species, the reduction of surface CeO_2 to Ce_2O_3 may also contribute to the reduction peak in the temperature range of $200\text{--}550^\circ\text{C}$. In addition, the peak reduction temperature changes with the $\text{Mn}_{0.5}\text{Ce}_{0.5}\text{O}_8$ loading. The second reduction peak in the temperature range of $690\text{--}800^\circ\text{C}$ can be assigned to the reduction of bulk CeO_2 and lattice oxygen. Fig. 4Ba-f exhibit the H_2 -TPR profiles of the $\text{Mn}_x\text{Ce}_{1-x}\text{O}_8/\text{3DOM-m SiO}_2$ catalysts with different metal contents. The as-prepared catalysts show various reduction peaks with different x values. When $x = 0$ (Fig. 4Ba), there are three reduction peaks in the temperature ranges of $400\text{--}500^\circ\text{C}$ (shoulder), $500\text{--}650^\circ\text{C}$, and $650\text{--}800^\circ\text{C}$. The reduction peaks are attributed to the reduction of surface adsorbed oxygen species and surface CeO_2 , bulk CeO_2 , and lattice oxygen, respectively [38]. With the increasing x value, the first reduction peak exhibits different shapes and peak temperatures. The peak reduction temperature decrease with the x value until $x = 0.8$. This may be due to the formation of composite oxides between Mn and Ce. When $x = 1$, a single reduction peak is present, which is located in the temperature range of $250\text{--}550^\circ\text{C}$, as shown in Fig. 4Bf, suggesting

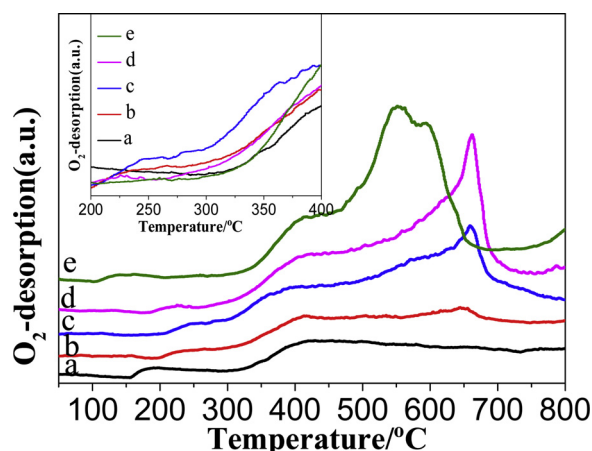


Fig. 5. O_2 -TPD profiles of the $Mn_xCe_{1-x}O_8/3DOM\text{-}m\text{ SiO}_2$ catalysts with different Ce to Mn molar ratios (a: $x = 0$; b: $x = 0.2$; c: $x = 0.5$; d: $x = 0.8$; e: $x = 1$).

the reduction of MnO_8 . The asymmetric peak hints that Mn^{4+} and Mn^{3+} may co-exist in the $MnO_8/3DOM\text{-}m\text{ SiO}_2$, which is also supported by the XRD results.

Except for the reducibility, the active oxygen species in the catalyst also plays an important role in soot combustion. Fig. 5 exhibits the O_2 -TPD profiles of as-prepared catalysts. Three oxygen desorption peaks, including $50^\circ\text{C} \leq T \leq 300^\circ\text{C}$, $300^\circ\text{C} \leq T \leq 500^\circ\text{C}$, and $500^\circ\text{C} \leq T \leq 800^\circ\text{C}$, are observed. The first range is assigned to surface active oxygen species (O_{surf}), which are originated from the oxygen vacancies [39]. The second is corresponding to the chemically adsorbed oxygen on the oxygen vacancies (O_2^-/O^-), which has strong interaction with the surface defects in the catalysts. The last is lattice oxygen (O^{2-}) and thus its desorption occurs at a relative high temperature, normally above 500°C [40]. It is noticed that an intense and sharp desorption peak appears around 660°C and grows with the Mn content in the $Mn_xCe_{1-x}O_8$ catalysts, which is in good agreement with the H_2 consumption in H_2 -TPR. In this work the soot catalytic combustion took place at $200\text{--}400^\circ\text{C}$, thus, the active oxygen species that desorb at $200\text{--}400^\circ\text{C}$ are important for enhancement of the catalytic activity. As shown in the insert of Fig. 5, the intensities of desorbed oxygen species from the samples are different from each other. The $Mn_{0.5}Ce_{0.5}O_8/3DOM\text{-}m\text{ SiO}_2$ catalyst has the largest amount of active oxygen species among all the samples, which agrees well with the catalytic activity.

3.1.5. Raman results of as-prepared catalysts

In order to study the interaction of Mn and Ce in as-prepared catalysts, Raman spectra of the $Mn_xCe_{1-x}O_8/3DOM\text{-}m\text{ SiO}_2$ catalysts were collected with a 532 nm laser, and the results are shown in Fig. 6. Two Raman peaks located at 630 and 443 cm^{-1} are observed in the Raman shift range of $150\text{--}1000\text{ cm}^{-1}$ when $Mn_{0.5}Ce_{0.5}O_8$ mixed oxide is loaded on 3DOM- $m\text{ SiO}_2$. The peak at 443 cm^{-1} can be ascribed to strong F_{2g} mode of CeO_2 fluorite phase. Compared with the pure CeO_2 (Fig. 6Ba), an obvious red shift (from 461 to 443 cm^{-1}) exists because of doping of Mn ions in the CeO_2 lattice. The peak at 630 cm^{-1} can be assigned to the Mn-O vibrations which are orthogonal and along the direction of the MnO_6 octahedral double chains [32]. Compared with Raman peaks of pure MnO_x (Fig. 6Bf), there is a red shift (about 5 cm^{-1}) for $Mn_{0.5}Ce_{0.5}O_8/3DOM\text{-}m\text{ SiO}_2$. In addition, to more clearly illustrate the interaction between Mn and Ce, Raman spectra of the $Mn_xCe_{1-x}O_8/3DOM\text{-}m\text{ SiO}_2$ catalysts with different Ce to Mn molar ratios are shown in Fig. 6B. With increasing x value, the Raman peaks for the $CeO_2 F_{2g}$ mode shifts from 461 to 441 cm^{-1} (Fig. 6Ba-d), also suggesting that Mn ions were doped into the CeO_2 lattice. When x value is 0.8, the Raman peak of CeO_2 disappears and one peak for MnO_x emerges, which is in good accordance with the XRD results (Fig. 2Be). When x value is 1,

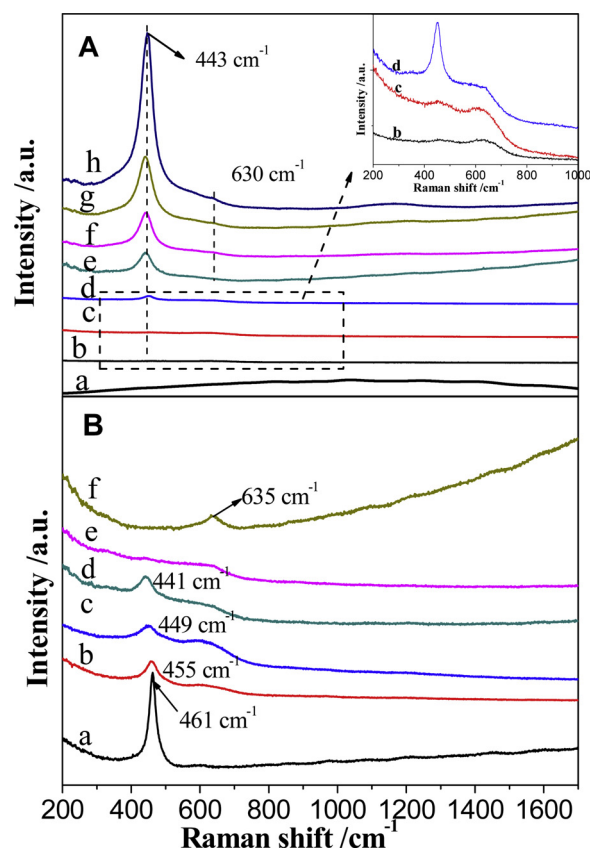


Fig. 6. Raman spectra of the $Mn_xCe_{1-x}O_8/3DOM\text{-}m\text{ SiO}_2$ catalysts with different $Mn_{0.5}Ce_{0.5}O_8$ loadings (A) and different Ce to Mn molar ratios (B). (A: a: 0%; b: 10%; c: 20%; d: 30%; e: 40%; f: 50%; g: 60%; h: 80%; B: a: $x = 0$; b: $x = 0.2$; c: $x = 0.4$; d: $x = 0.6$; e: $x = 0.8$; f: $x = 1$).

$MnO_8/3DOM\text{-}m\text{ SiO}_2$ exhibits a Raman peak at 635 cm^{-1} owing to vibration of Mn-O bonds. Based on the Raman results, it can be inferred that Mn and Ce elements have completely mixed at the atomic level and formed perfect mixed oxides. The $MnO_x\text{-}CeO_2$ composite oxides are expected to enhance catalytic performance for soot combustion.

As reported previously, UV Raman (325 nm) can probe defect sites especially when other metals adopted in the cerium oxides [23,41]. Figure S3A exhibits the UV Raman spectra and the concentration of surface oxygen vacancies of the $Mn_xCe_{1-x}O_8/3DOM\text{-}m\text{ SiO}_2$ catalysts with different Ce to Mn molar ratios. Compared with the visible Raman spectra, two new bands located at around 590 cm^{-1} and 1170 cm^{-1} are observed. The former is from the defect sites (O-vacancies) and the latter, second-order longitudinal optical (2LO) mode [42]. The peak area ratio between the 570 cm^{-1} (A_1) and 456 cm^{-1} (A_2) peaks is known to reflect the abundance of the oxygen vacancies created by the replacement of Ce atoms by Mn in the $Mn_xCe_{1-x}O_8$ mixed oxide [41]. To clearly compare the difference in the O-vacancies among the as-prepared catalysts, the A_1 to A_2 ratios were calculated and are presented in Figure S3B. When x value is 0.5, the $Mn_xCe_{1-x}O_8/3DOM\text{-}m\text{ SiO}_2$ has the highest A_1 to A_2 ratio, which means that it has the largest amount of O-vacancies among the catalysts.

3.1.6. XPS results of as-prepared catalysts

To probe the chemical states of Mn and Ce ions, the $Mn_xCe_{1-x}O_8/3DOM\text{-}m\text{ SiO}_2$ catalysts with different Ce to Mn molar ratios were characterized by XPS, and the results are exhibited in Fig. 7 and summarized in Table S1. As shown in Fig. 7A, the Ce 3d XPS spectra are rather complex and can be assigned to $3d_{3/2}$ spin-orbit states (labeled with “u”) and $3d_{5/2}$ states (labeled with “v”). The peaks labeled as u”, u and v”, v are assigned to $Ce^{4+} 3d_{3/2}$ and $Ce^{4+} 3d_{5/2}$,

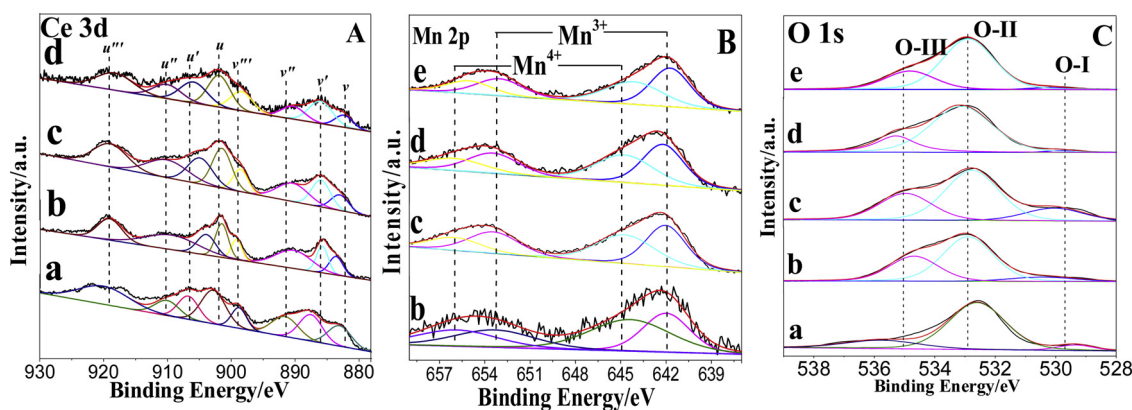


Fig. 7. XPS spectra of the $\text{Mn}_x\text{Ce}_{1-x}\text{O}_8/3\text{DOM-m SiO}_2$ catalysts with different Ce to Mn molar ratios (a: $x = 0$; b: $x = 0.2$; c: $x = 0.5$; d: $x = 0.8$; e: $x = 1$).

respectively, and u' and v' are assigned to $\text{Ce}^{3+} 3d_{3/2}$ and $\text{Ce}^{3+} 3d_{5/2}$, respectively [43]. When Mn ions are incorporated into the CeO_2 lattice, an obvious shift of bonding energy can be found (as shown in Fig. 7Aa and b, c, d). The results in Table S1 indicate that the relative intensity of Ce^{3+} increases with the Mn content. Generally speaking, higher Ce^{3+} content creates more charge imbalance and stronger oxygen storage capacity with the latter leading to an increase in active oxygen on the catalyst surface. Fig. 7B exhibits the Mn 2p XPS spectra of the $\text{Mn}_x\text{Ce}_{1-x}\text{O}_8/3\text{DOM-m SiO}_2$ catalysts. Two kinds of Mn species, Mn^{3+} (ca. 642 eV), and Mn^{4+} (645 eV) are present in the sample from XPS spectra [44]. Meanwhile, the Mn $2p_{1/2}$ peaks also show two kinds of Mn species with a BE range of 650–655 eV. Both XRD (Fig. 2) and XPS results suggest that the Mn ions are incorporated into the CeO_2 lattice. No significant shift in binding energy is found in the Mn 2p XPS spectra. According to the results shown in Table S1, the interaction between Mn and Ce has an influence on the partition between Mn^{3+} and Mn^{4+} . The portion of Mn^{4+} increases with the Ce content in the $\text{Mn}_x\text{Ce}_{1-x}\text{O}_8$. As shown in Fig. 7C, the O1s peaks can be separated into O-I, O-II and O-III, whose binding energies are 528.0–530.0, 532.0–533.0, and 534.0–535.0 eV, respectively. The O-I is attributed to lattice oxygen ions, having property related to metal-oxygen bonds. In the as-prepared catalysts, the O-I may come from Mn-O, Ce-O, Ce-O-Mn, Ce-Mn-O, or some Si-O-Mn and Si-O-Ce bonds. When the metals oxides are supported on 3DOM-m SiO_2 , the O-I peaks are different. The shift in binding energy for the O-I can be obtained in the $\text{CeO}_2/\text{SiO}_2$ (Fig. 7Ca). As shown in Table S1, the portion of the O-I increases when $\text{Mn}_x\text{Ce}_{1-x}\text{O}_8$ is loaded on 3DOM-m SiO_2 . When x value is 0.5 in the $\text{Mn}_x\text{Ce}_{1-x}\text{O}_8$, the portion of the O-I reaches the largest value. The O-II, which is the dominating component in the O1s peaks, is related to O^{2-} species in SiO_2 (Si-O-Si environments) [45]. The O-III component located at ~535 eV may include contributions from the surface Si-O or Si-OH.

3.2. Catalytic performance for soot combustion

3.2.1. Catalytic activity of as-prepared catalysts

Table 3 summarizes the catalytic performance of as-prepared catalysts for soot oxidation. For better comparison, non-catalytic soot combustion as well as combustion over 3DOM SiO_2 and 3DOM-m SiO_2 were also tested. As shown in Table 3, the T_{10} , T_{50} , and T_{90} for non-catalytic soot combustion are 408, 539, and 584 °C, respectively. 3DOM SiO_2 exhibits weak catalytic activity for soot combustion, and the T_{10} , T_{50} , and T_{90} are 312, 490, and 555 °C, respectively. Due to ordered mesopores in the skeleton of SiO_2 , the contact effect of reaction gases (O_2 and NO) for 3DOM-m SiO_2 is higher than that of 3DOM SiO_2 . This explains the higher catalytic activity of 3DOM-m SiO_2 , whose T_{10} , T_{50} , and T_{90} are 296, 460, and 524 °C, respectively. When the active components are supported on 3DOM-m SiO_2 , the as-prepared catalysts exhibit good catalytic performance for soot combustion. $\text{Mn}_x\text{Ce}_{1-x}\text{O}_8/$

Table 3

Catalytic performances of as-prepared catalysts for soot combustion.

Catalysts	T_{10}	T_{50}	T_{90}	$S_{\text{CO}_2}/\%$
Soot	408	539	584	49.2
3DOM SiO_2	312	490	555	69.1
3DOM-m SiO_2	296	460	524	78.1
$\text{CeO}_2/3\text{DOM-m SiO}_2$	291	366	406	96.5
$\text{Mn}_{0.2}\text{Ce}_{0.8}\text{O}_8/3\text{DOM-m SiO}_2$	281	353	391	98.8
$\text{Mn}_{0.4}\text{Ce}_{0.6}\text{O}_8/3\text{DOM-m SiO}_2$	282	351	390	99.1
$\text{Mn}_{0.6}\text{Ce}_{0.4}\text{O}_8/3\text{DOM-m SiO}_2$	276	356	394	98.9
$\text{Mn}_{0.8}\text{Ce}_{0.2}\text{O}_8/3\text{DOM-m SiO}_2$	285	356	396	99.4
$\text{MnO}_8/3\text{DOM-m SiO}_2$	296	372	412	97.3
10% $\text{Mn}_{0.5}\text{Ce}_{0.5}\text{O}_8/3\text{DOM-m SiO}_2$	286	368	408	97.5
20% $\text{Mn}_{0.5}\text{Ce}_{0.5}\text{O}_8/3\text{DOM-m SiO}_2$	284	356	393	98.9
30% $\text{Mn}_{0.5}\text{Ce}_{0.5}\text{O}_8/3\text{DOM-m SiO}_2$	281	351	388	99.1
40% $\text{Mn}_{0.5}\text{Ce}_{0.5}\text{O}_8/3\text{DOM-m SiO}_2$	278	346	384	99.2
50% $\text{Mn}_{0.5}\text{Ce}_{0.5}\text{O}_8/3\text{DOM-m SiO}_2$	275	345	382	99.2
60% $\text{Mn}_{0.5}\text{Ce}_{0.5}\text{O}_8/3\text{DOM-m SiO}_2$	272	339	376	99.2
80% $\text{Mn}_{0.5}\text{Ce}_{0.5}\text{O}_8/3\text{DOM-m SiO}_2$	270	342	378	99.2
40% $\text{Mn}_{0.5}\text{Ce}_{0.5}\text{O}_8/3\text{DOM SiO}_2$	285	349	388	99.1
40% $\text{Mn}_{0.5}\text{Ce}_{0.5}\text{O}_8/\text{silica gel}$	300	387	453	95.6
3DOM $\text{Mn}_{0.5}\text{Ce}_{0.5}\text{O}_8$	297	358	396	94.2
Powder $\text{Mn}_{0.5}\text{Ce}_{0.5}\text{O}_8$	299	364	400	96.9

3DOM-m SiO_2 catalysts with different compositions have various catalytic activities. Firstly, the catalytic activity increases with the x value until $x = 0.5$, and then it decreases with the x value. These results indicate that the interaction between Mn and Ce has positive influence on soot combustion. In order to get the best catalyst performance, the catalytic activities of $\text{Mn}_{0.5}\text{Ce}_{0.5}\text{O}_8/3\text{DOM-m SiO}_2$ with different $\text{Mn}_{0.5}\text{Ce}_{0.5}\text{O}_8$ loadings were also determined. From Table 3, it can be seen that the catalytic activity of $\text{Mn}_{0.5}\text{Ce}_{0.5}\text{O}_8/3\text{DOM-m SiO}_2$ firstly increases with the $\text{Mn}_{0.5}\text{Ce}_{0.5}\text{O}_8$ loading, and then stays constant, even when the $\text{Mn}_{0.5}\text{Ce}_{0.5}\text{O}_8$ loading is further increased. This is probably because the pore structure of SiO_2 and $\text{Mn}_{0.5}\text{Ce}_{0.5}\text{O}_8$ active components have reached certain state of equilibrium. In consideration of the pore structure of SiO_2 and the loading of $\text{Mn}_{0.5}\text{Ce}_{0.5}\text{O}_8$, 40% $\text{Mn}_{0.5}\text{Ce}_{0.5}\text{O}_8/3\text{DOM-m SiO}_2$ appears to be a good choice for soot combustion. In order to further investigate macropore and mesopore effect on soot combustion, the catalytic activities of 40% $\text{Mn}_{0.5}\text{Ce}_{0.5}\text{O}_8/3\text{DOM SiO}_2$, powder $\text{Mn}_{0.5}\text{Ce}_{0.5}\text{O}_8$ and 40% $\text{Mn}_{0.5}\text{Ce}_{0.5}\text{O}_8/\text{silica gel}$ were tested and the results are shown in Table 3. 40% $\text{Mn}_{0.5}\text{Ce}_{0.5}\text{O}_8/3\text{DOM SiO}_2$ shows somewhat lower catalytic activity than that of 40% $\text{Mn}_{0.5}\text{Ce}_{0.5}\text{O}_8/3\text{DOM-m SiO}_2$, indicating that the mesoporous structure is favorable for soot combustion. In addition, 40% $\text{Mn}_{0.5}\text{Ce}_{0.5}\text{O}_8/\text{silica gel}$ shows much lower catalytic activity than that of 40% $\text{Mn}_{0.5}\text{Ce}_{0.5}\text{O}_8/3\text{DOM-m SiO}_2$ indicating that the 3DOM structure is favorable for soot combustion. The lower catalytic activity of powder $\text{Mn}_{0.5}\text{Ce}_{0.5}\text{O}_8$ catalyst also suggests that pore structure is important for soot combustion. In addition, the pure 3DOM $\text{Mn}_{0.5}\text{Ce}_{0.5}\text{O}_8$ catalyst also exhibits lower activity than

40% $\text{Mn}_{0.5}\text{Ce}_{0.5}\text{O}_8/3\text{DOM-m SiO}_2$ [37]. Based on the above results, it can be concluded that the loading of Mn-Ce mixed oxides and porous structure significantly affect catalytic activities of as-prepared catalysts for soot combustion.

The 40% $\text{Mn}_{0.5}\text{Ce}_{0.5}\text{O}_8/3\text{DOM-m SiO}_2$ catalyst was also examined for stability and the results are shown in Figure S4. After five-cycles, 40% $\text{Mn}_{0.5}\text{Ce}_{0.5}\text{O}_8/3\text{DOM-m SiO}_2$ still maintains good catalytic performance, and T_{10} , T_{50} , and T_{90} are 277 ± 2 , 346 ± 2 and 385 ± 2 °C, respectively. Meanwhile, CO_2 selectivity is also higher than 95%. In our previous studies, the mechanical strength of 3DOM SiO_2 was well demonstrated [25,32]. In this work, besides the macroporous effect, the mesopore structure of 3DOM-m SiO_2 also plays an important role for high catalytic activity. Therefore, we performed measurements of pore size distribution and XRD on the used 40% $\text{Mn}_{0.5}\text{Ce}_{0.5}\text{O}_8/3\text{DOM-m SiO}_2$ catalyst. As shown in Figure S4B, the used 40% $\text{Mn}_{0.5}\text{Ce}_{0.5}\text{O}_8/3\text{DOM-m SiO}_2$ catalyst still maintains good mesoporous structure after five-cycles. In addition, as active components, the Mn-Ce mixed oxides play a decisive role for the high catalytic performance. Interestingly, the similarity of XRD diffraction patterns for the used and fresh catalysts indicates that the crystal form of Mn-Ce mixed oxides remains very well during soot combustion (Figure S4C). Based on the above characterization, it can be concluded that the $\text{Mn}_{0.5}\text{Ce}_{0.5}\text{O}_8/3\text{DOM-m SiO}_2$ catalysts have good thermal and activity stability for soot combustion.

3.2.2. Catalytic performance with the presence of NO

As a reactant, NO plays an important role in soot combustion. To research the influence of NO, the catalytic activities of 40% $\text{Mn}_{0.5}\text{Ce}_{0.5}\text{O}_8/3\text{DOM-m SiO}_2$ with various NO concentrations were tested and the results are shown in Fig. 8. As a general observation, NO has a significant effect on catalytic activities. When NO is absent, the catalyst exhibits lower catalytic activity, and the T_{10} , T_{50} , and T_{90} are

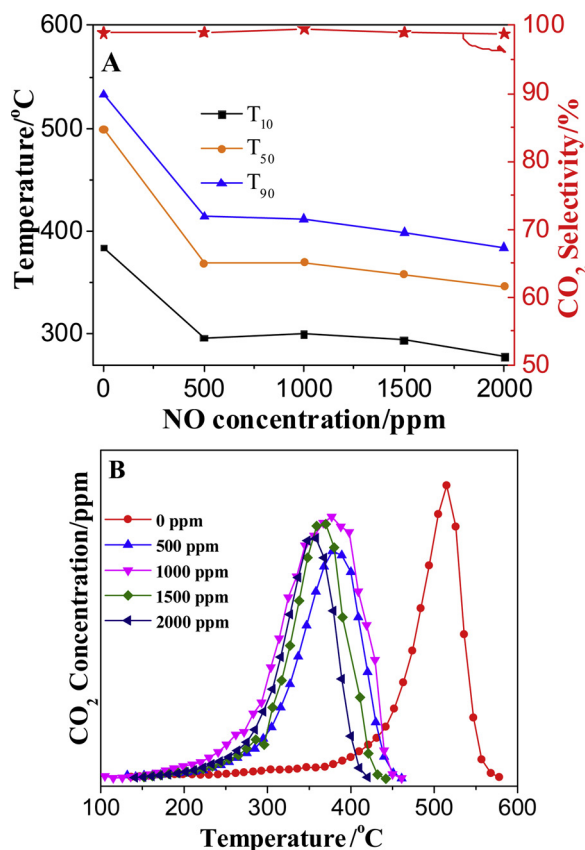


Fig. 8. Catalytic activities and CO_2 concentration profiles of the 40% $\text{Mn}_{0.5}\text{Ce}_{0.5}\text{O}_8/3\text{DOM-m SiO}_2$ catalyst at different NO concentrations.

384, 499, and 533 °C, respectively. The catalytic performance is greatly enhanced when NO is present. The T_{10} , T_{50} , and T_{90} decrease to 296, 369, and 414 °C when the NO concentration is 500 ppm. With the increasing of NO concentration, the catalytic activity does not change much, and the T_{10} , T_{50} , and T_{90} are 295 ± 5 , 364 ± 6 , and 407 ± 7 °C, respectively. With further increasing of NO concentration (up to 2000 ppm), the catalytic activity has only a minor enhancement, and the T_{10} , T_{50} , and T_{90} arrive at 278, 346, and 384 °C, respectively. To further illustrate the influence of NO, the profiles of CO_2 concentration at different NO concentrations are also exhibited in Fig. 8B. The difference in CO_2 concentration profiles with and without NO suggests that NO has a great promotion effect on the catalytic activities for soot oxidation. However, the CO_2 selectivity is not influenced by NO, and the value keeps higher than 98% regardless of the presence of NO. Many previous reports demonstrated that NO could be catalytically oxidized to NO_2 [46]. Because of high oxidizing ability of NO_2 , soot particles will react with NO_2 instead of O_2 . Therefore, the catalytic activities will improve with higher level of NO. However, the changing trend for catalytic performance of as-prepared catalysts does not agree with our previous report [25]. This is probably due to the mesopores in 3DOM-m SiO_2 support, which will be explained in more detail later.

3.2.3. Sulfur and water-resistance of as-prepared catalysts

The presence of sulfur compounds in diesel fuels and water vapor in the exhaust gas are nearly unavoidable. Therefore, the tolerance of sulfur dioxide and water by the catalysts is significant for applications in diesel exhaust treatment. In this work, the catalytic performance at different concentrations of SO_2 and water vapor (10%) were tested and the results are shown in Figs. 9 and S5. As shown in Fig. 9A, the T_{10} , T_{50} , and T_{90} of 40% $\text{Mn}_{0.5}\text{Ce}_{0.5}\text{O}_8/3\text{DOM-m SiO}_2$ greatly increase while CO_2 selectivity decreases when 50 ppm SO_2 is present. With the increasing of SO_2 concentration, the values of T_{10} , T_{50} , and T_{90} slowly raise while the CO_2 selectivity first decreases until SO_2 reaches 100 ppm and then remains constant. Form the CO_2 concentration profiles

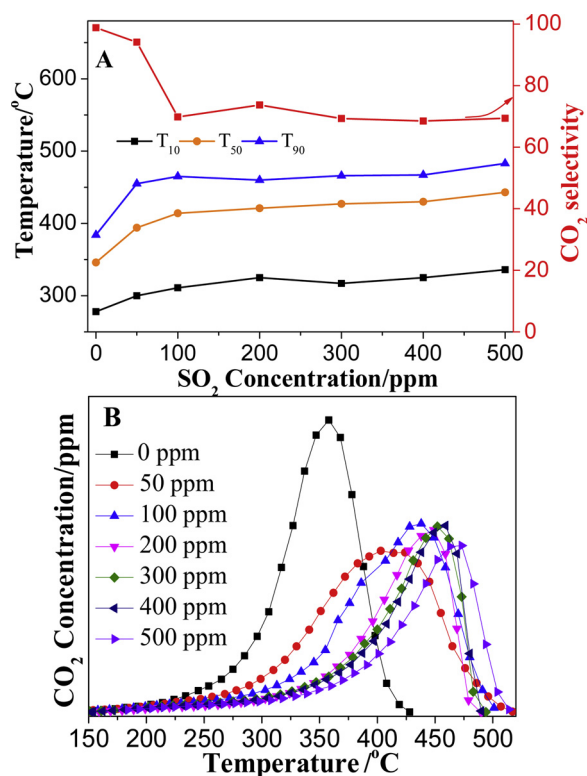


Fig. 9. Catalytic activities (A) and CO_2 concentration profiles (B) of the 40% $\text{Mn}_{0.5}\text{Ce}_{0.5}\text{O}_8/3\text{DOM-m SiO}_2$ catalyst at different SO_2 concentrations.

(Fig. 9B), it also can be seen that the CO_2 profiles move to higher temperature range when SO_2 is present. As shown in Figure S5A, the addition of water vapor (10%) has little effect on the catalytic activities of as-prepared catalysts. Interestingly, when both low concentrations of SO_2 (100 ppm) and water vapor (10%) are present, the as-prepared catalysts exhibit higher catalytic activities than when only SO_2 is there. However, when the concentrations of SO_2 is increased, the catalytic activities of as-prepared catalysts are similar. To investigate the stability of as-prepared catalysts, the catalytic performance of the catalysts with presulfurization and hydrothermal treatments were also investigated and the results are presented in Figure S5. The presulfurization has some influence on the catalytic activity, which means the as-prepared catalysts exhibit some SO_2 resistance. However, the hydrothermal treatment has a major impact on the catalytic activity. Combined with the results in Figure S1, it is speculated that the diameter of the $\text{Mn}_{0.5}\text{Ce}_{0.5}\text{O}_8$ nanoparticles is one of the determining factors for catalytic activity. In addition, the CO_2 concentration profiles (Figure S5B) also demonstrate the same trend.

Figure S6 shows images of the 40% $\text{Mn}_{0.5}\text{Ce}_{0.5}\text{O}_8/3\text{DOM-m SiO}_2$ catalyst after reaction with the presence of different concentrations of SO_2 and water vapor (10%). The colors are different among them. When there was no SO_2 , it is black, suggesting the presence of manganese oxides. When SO_2 was present, it transitions from black to white with increasing of SO_2 concentration. This phenomenon indicates that the active components were chemically changed by sulfonation of SO_2 . However, the sulfur tolerance of as-prepared catalysts has been enhanced compared to that of single active component catalysts owing to the formation of $\text{Mn}_x\text{Ce}_{1-x}\text{O}_8$ mixed oxides between Mn and Ce. In addition, as shown in Figures S6h and i, when 10% water vapor is present, 40% $\text{Mn}_{0.5}\text{Ce}_{0.5}\text{O}_8/3\text{DOM-m SiO}_2$ catalyst remains black, indicating that the active manganite component is also sustained (Figure S6h). However, when both SO_2 (300 ppm) and water vapor (10%) are introduced, the color of the catalyst has changed to grey owing to sulfonation of SO_2 for manganite (Figure S6i).

To find the reasons for sulfur and water tolerance of as-prepared catalysts, the physical properties of 40% $\text{Mn}_{0.5}\text{Ce}_{0.5}\text{O}_8/3\text{DOM-m SiO}_2$ catalyst after reaction at different SO_2 concentrations and water vapor (10%) were characterized by XRD and Raman spectroscopy. The characterization results are shown in Fig. 10. From the XRD results (Fig. 10A), the intensity of CeO_2 diffraction peak is enhanced with increasing of SO_2 concentration. In addition, a slight 2θ angle shift from 28.7° to 28.6° is also observed in the insert of Fig. 10A. Considering the XRD results in Fig. 2A and the color of catalyst in Figure S6, it is inferred that manganese component had reacted with SO_2 and formed manganese sulfate species. However, cerium component remains in the oxide form. In order to further support the above inference, the corresponding Raman spectra were measured and the results are shown in Fig. 10B. An obvious Raman blue shift from 441 to 461 cm^{-1} is observed when the SO_2 concentration increases from 0 to 500 ppm. In addition, the Raman peak of Mn-O disappears and new Raman peaks at 1002 and 1018 cm^{-1} emerge and their intensities enhance with the increasing of SO_2 concentration. As reported in the literature, the emerging Raman peaks can be assigned to vibration of S–O bonds [47]. In addition, as shown in Fig. 10C and D, after reaction in the presence of the 10% water vapor, the catalyst shows similar XRD patterns and Raman spectra to those when there was no water. When both water and SO_2 are introduced, the diffraction peaks and Raman shift of the catalyst are similar to those when only SO_2 is present. The emerging Raman peaks at 1002 and 1018 cm^{-1} also show the sulfonation of as-prepared catalysts. Considering the Raman peaks in Fig. 6, it is confirmed that active component of cerium remains in the oxide form while active manganese component changes from oxides to sulfate species when SO_2 is present in soot combustion. When manganese is mixed with cerium and forms $\text{Mn}_x\text{Ce}_{1-x}\text{O}_8$ mixed oxides, the sulfur tolerance of the catalysts is enhanced to some extent [48]. Based on the above results, it is suggested that active manganese component is less stable and easier to

react with SO_2 than cerium. However, when both water and SO_2 are present, the as-prepared catalysts exhibit higher catalytic activities than when there is only SO_2 at low levels.

3.3. Probable reaction mechanism for soot combustion

In a gas-solid-solid reaction such as catalytic soot combustion, catalytic performance is affected by activation of gas molecules and contact between soot and catalyst particles. In fact, our previous studies have demonstrated that 3DOM materials with uniform pore size and periodic voids exhibit higher catalytic activities than corresponding powder materials [16,17,24,25,37]. In this work, in order to improve the contact efficiency, the catalysts with 3DOM structure were designed and synthesized. In this 3DOM structure the number of available active sites can be maximized, especially internal active sites. In addition, the uniform macroporous network allows efficient mass transfer with small diffusional resistance when large size reactants such as soot particles go through the catalyst structure. Besides enhancing contact efficiency by 3DOM structure, the ordered mesoporous structure of the catalyst was designed and successfully prepared for the activation of gas molecules in this work. The incipient wetness impregnation method for catalyst preparation disperses the active components throughout the macroporous and mesoporous structures. As shown in Fig. 11, the reactant gases not only spread in the macropores but also enter into the ordered mesopores. Due to long residing time in the mesopores, the reactant gases, including NO and O_2 , can sufficiently react with each other and form NO_2 . The strong oxidizing NO_2 can react with soot directly. Based on the results in Table 3, the catalytic activities have major improvement owing to macroporous and mesoporous structures. Therefore, it is significantly important to study and design 3DOM-m structure for soot combustion.

Except for the above structural effects, the intrinsic activity of the catalysts is another important factor for enhancing the catalytic activity owing to deep oxidation reaction for soot combustion. The results of catalytic performance have demonstrated that $\text{Mn}_x\text{Ce}_{1-x}\text{O}_8$ mixed oxides with different Mn and Ce molar ratios exhibit different catalytic activities. This phenomenon illustrates the synergistic effect between Mn and Ce. Generally speaking, ceria has strong oxygen storage property in the catalytic reactions while manganese oxides exhibit high NO_x adsorption capacity. Therefore, tuning Mn and Ce molar ratio can maximize their catalytic activities. In addition, Raman and XRD results have proved that Mn ions were completely incorporated into the CeO_2 lattice in $\text{Mn}_x\text{Ce}_{1-x}\text{O}_8$ mixed oxides. The results of UV-Raman (Figure S3) and DFT calculation (Figs. 12 and S7, more discussion later) indicate that the doping effect increases the number of oxygen vacancies and enhances active oxygen transport. In order to further study the reaction mechanism, the DFT calculation, which is related to the formation of oxygen vacancies and activation of oxygen species on the $\text{Mn}_x\text{Ce}_{1-x}\text{O}_8$ mixed oxides, was carried out by the VASP. As shown in Figs. 12 and S7, when Mn atom is doped into cerium oxide, the Mn atom coordinates with one bulk oxygen atom and three surface oxygen atoms. The bond distances of cerium and oxygen are in a range of $2.35\text{ \AA} \sim 2.36\text{ \AA}$, while the bond distances of manganese and oxygen are in a range of $1.92\text{ \AA} \sim 1.96\text{ \AA}$. Significant structural changes occur on the surface of cerium oxide when Mn atom is doped. Based on the calculation, we found that oxygen vacancy formation energy in cerium oxide is 2.47 eV , while oxygen vacancy formation energy is only 0.08 eV when Mn atom is doped. It indicates that the doping of manganese atoms is beneficial to the formation of oxygen vacancies and is conducive to adsorption of oxygen for subsequent reactions. When oxygen vacancies form, the magnetic moment of the manganese atom is $3.87\text{ }\mu\text{B}$, indicating an oxidation state of +3 resulting from one electron being transferred from O^{2-} (orange oxygen atom) to Mn^{4+} . When dioxygen is adsorbed to the oxygen vacancies, the bond length in the oxygen molecule changes from 1.24 \AA to 1.33 \AA , indicating that O_2 gets an electron from Ce^{3+} and forms O_2^- [49]. Thus, acting together by the

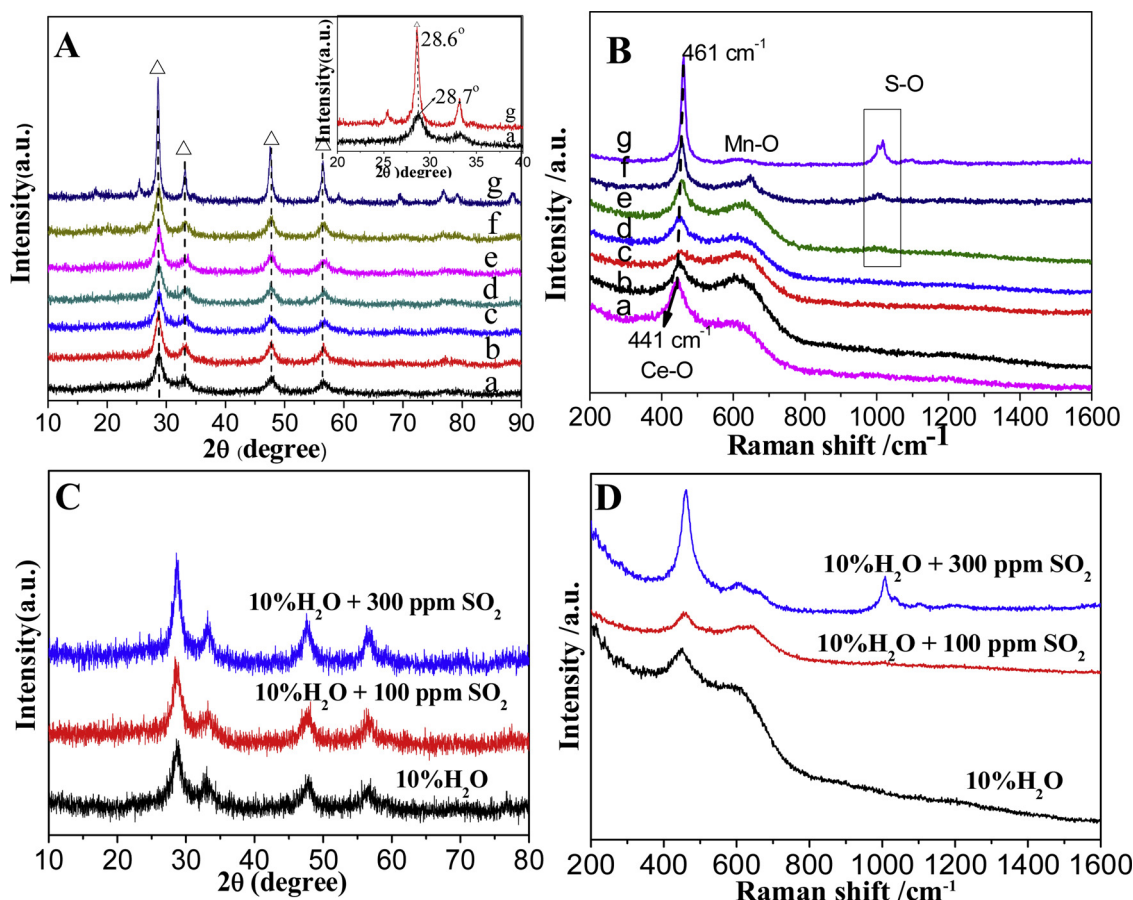


Fig. 10. X-ray diffraction patterns (A, C) and Raman spectra (B, D) of the 40% $\text{Mn}_{0.5}\text{Ce}_{0.5}\text{O}_8/3\text{DOM-m SiO}_2$ catalyst after reaction at different SO_2 and H_2O concentrations.

(a: 0 ppm; b: 50 ppm; c: 100 ppm; d: 200 ppm; e: 300 ppm; f: 400 ppm; g: 500 ppm).

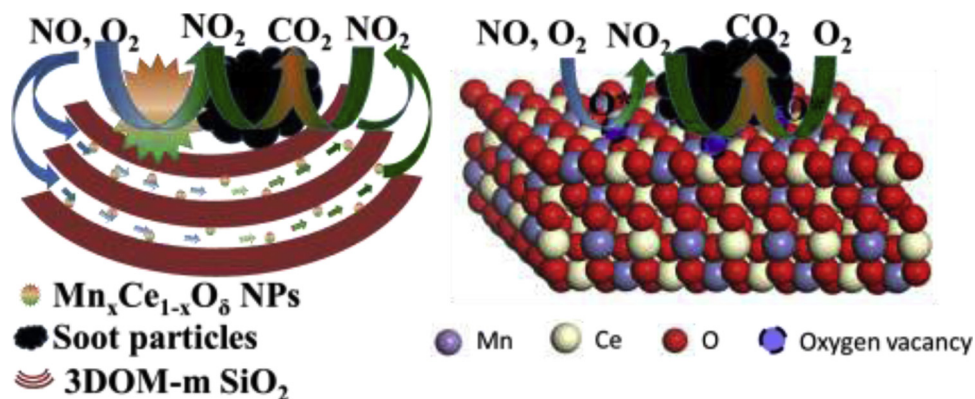


Fig. 11. Probable reaction mechanism on the as-prepared catalysts.

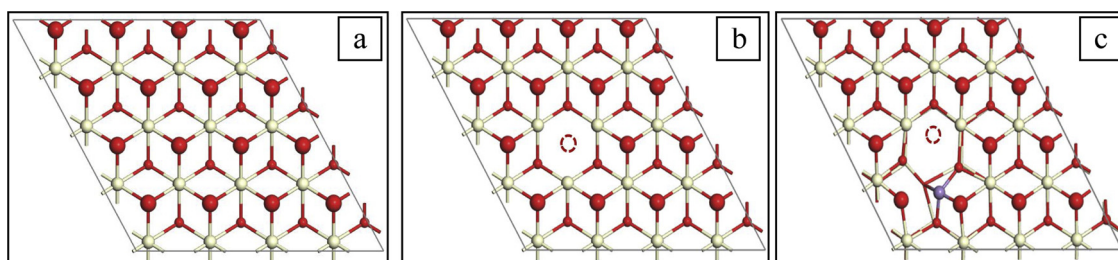
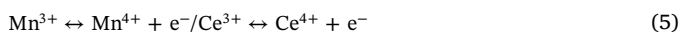
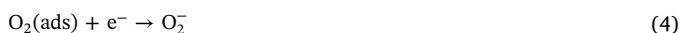
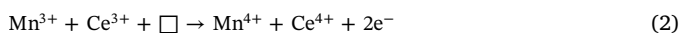
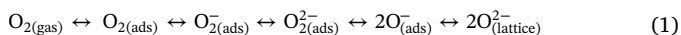


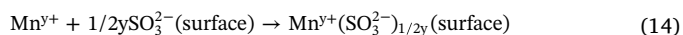
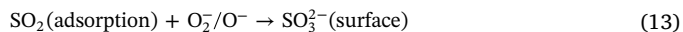
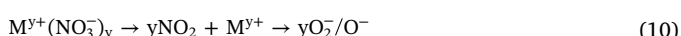
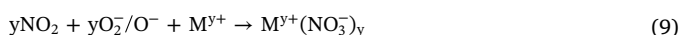
Fig. 12. Structure of $\text{CeO}_2(111)$ (a,b) and $\text{MnCe}_{x-1}\text{O}_{2x}(111)$ (c) surfaces. (The oxygen vacancy is represented by "○"). Color scheme: red: O; white: Ce; purple: Mn).

cerium atom and manganese atom is more conducive to the activation of oxygen species.

In this work, based on the results of O₂-TPD, UV-Raman, XPS, DFT calculation and other characterization results, a probable soot combustion mechanism on as-prepared catalysts is proposed and described in the following. As described in Reaction 1, there are many kinds of oxygen species on the oxides [23]. From the XPS results (Fig. 7) and DFT calculation (Figs. 12 and S7), the two electrons derived from the formation of an oxygen vacancy can be accepted by adjacent Ce⁴⁺ or Mn⁴⁺ to form Ce³⁺ or Mn³⁺ (Reaction 2). During the activation of gaseous dioxygen, it first adsorbs on an oxygen vacancy (“□”) close to the Ce³⁺ or Mn³⁺ and forms adsorbed oxygen (Reaction 3) [50]. Subsequently, the adsorbed oxygen obtains an electron from Ce³⁺ or Mn³⁺ and form O₂[−] and Ce⁴⁺ or Mn⁴⁺ by redox reaction of Mn³⁺/Mn⁴⁺ and Ce³⁺/Ce⁴⁺ (Reactions 4 and 5). After that, the O₂[−] may further capture an electron and disintegrate into two O[−] (Reaction 6). Then, the O₂[−]/O[−] migrate away from the active sites and come in contact with soot particles inside the macropores. Due to their high oxidizing ability, these O₂[−]/O[−] species react with soot particles and form CO and CO₂ when NO is absent in the reaction system (Reaction 7) [51]. In addition, the macropores in the 3DOM structure would enhance the diffusion efficiency of soot particles and reduce the transport distance of active oxygen species, thus the catalytic performance is improved.



Things are different when NO is present in the reaction system. As shown in Reaction 8, some of the active oxygen species react with NO and form NO₂ (Reaction 8), and then NO₂, a strong oxidant, adsorbs on the surface of soot and oxidizes carbon on the soot [52]. Besides engaging in the direct oxidation of soot, NO₂ also can be stored by formation of bidentate/monodentate nitrates on the metal sites (M^{y+} means Mn^{y+} or Ce^{y+} in Reaction 9, the value of y is 3 or 4) when the temperature is low [53]. When the temperature is higher, these bidentate/monodentate nitrates species may decompose and release NO₂ (Reaction 10). After that, the released NO₂ may react with soot and produce CO or CO₂ (Reaction 11). This storage/release mechanism of NO_x has been demonstrated by many previous studies. [54] Research indicates that the nitrate storage capacity of MnO_x-CeO₂ is three to five times higher than that of the individual oxides with strong ability to release NO₂ [55]. This pathway with storage/release of NO_x results in a change of reaction mechanism in the process of soot oxidation, from a solid(soot)-solid(catalyst)-gas(O₂) system to a solid(soot)-gas(NO₂)-gas(O₂) system [56]. Due to this change, the catalytic performance of the as-prepared catalysts have been greatly improved when NO participates in the process of soot combustion (Fig. 8). Besides the NO₂-assisted mechanism, the active oxygen mechanism (mentioned earlier) also takes place when NO is present in the reaction system, even if it may not play a leading role.



Based on the results of sulfur-resistance in Part 3.2, it is suggested that as-prepared catalysts exhibit some sulfur tolerance. The XRD and Raman results illustrate that sulfate species (especially for manganese sulfate) were formed when the SO₂ was present in the reaction gases. The probable formation mechanism is as follows. Firstly, the gaseous SO₂ is adsorbed on the surface of Mn_xCe_{1-x}O₈ mixed oxides and forms adsorbed SO₂ (Reaction 12). After that, the adsorbed SO₂ reacts with O[−] (activated) species and forms sulfate/sulfite species (Reaction 13). The SO₂ readily combines with manganese and forms manganese sulfate owing to its stronger affiliation with Mn than Ce (Reaction 14). The formation of manganese sulfate/sulfite species will lead to lower catalytic activity. However, owing to the formation of Mn_xCe_{1-x}O₈ mixed oxides, the synergistic effect between Mn and Ce is now in favor of maintaining catalytic activity. As shown in Figs. 9 and S5, the catalytic activity of as-prepared catalyst is relatively stable, even though SO₂ content increases to a high level in the reaction. When water vapor is present in the reaction, the sulfate species would react with water and transform to H₂SO₄. At high temperatures (> 340 °C), the generated H₂SO₄ may evaporate. Therefore, when water vapor is present in the reaction gases, the as-prepared catalysts exhibit higher catalytic activities than when there is only SO₂ in the reaction gases.

4. Conclusions

In summary, a series of Mn_xCe_{1-x}O₈/3DOM-m SiO₂ catalysts with different Mn_{0.5}Ce_{0.5}O₈ loadings and different x values were purposefully designed and successfully prepared by a very simple method. The as-prepared catalysts contain 3DOM structure embedded with ordered mesoporous structure. The average diameters of macropores and mesopores are about 330 and 5 nm, respectively. The Mn_xCe_{1-x}O₈/3DOM-m SiO₂ catalysts were used in soot combustion reaction and exhibited high catalytic activities. Compared with non-catalytic soot combustion and combustion over 3DOM-m SiO₂, the T₁₀, T₅₀, and T₉₀ of Mn_xCe_{1-x}O₈/3DOM-m SiO₂ catalysts are remarkably lower. Moreover, the catalysts exhibited high catalytic stability for soot combustion. The characterization results also proved that the physicochemical properties of the used catalysts are similar to that of the fresh counterparts. Based on the analyses of reaction mechanisms, the good catalytic performance is attributed to the simultaneous presence of macropores and mesopores and synergistic effects between Mn and Ce. The sulfur tolerance of as-prepared catalysts can be enhanced to some extent by forming Mn_xCe_{1-x}O₈ mixed oxides, and the reasons for sulfur tolerance have been well illustrated in this paper. Therefore, concepts for design and synthesis of novel catalysts of Mn_xCe_{1-x}O₈/3DOM-m SiO₂ for soot combustion are proposed. More importantly, this work will aid rational design and facile preparation of highly efficient catalysts for the reactions between large solid particles and small gas molecules.

Acknowledgments

This work was financially supported by NSFC (21603149, 21761162016); The Liaoning Province Overseas (National) Cooperation Training Project of High Level Innovation Team (2018LNGXGJWPY-YB026); Support Program for Young and Middle-aged Scientific and Technological Innovation Talents of Shenyang, (RC170161); Liaoning Province Colleges and Universities Innovative Talents Support Plan (LR2016029); Open Topic for Beijing University of Chemical Technology State Key Laboratory of Chemical Resource Engineering, (CRE-2017-C-306). This work was partially supported by the Research Grants Council (RGC) of Hong Kong through NSFC/RGC Joint Research Scheme (RGC Project No. N_CUHK451/17). Engineering

Technology Research Center of Catalysis for Energy and Environment, Major Platform for Science and Technology of the Universities in Liaoning Province.

Appendix A. Supplementary data

Supplementary material related to this article can be found, in the online version, at doi:<https://doi.org/10.1016/j.apcatb.2019.04.097>.

References

- [1] G.C. Dhal, D. Mohan, R. Prasad, Preparation and application of effective different catalysts for simultaneous control of diesel soot and NO_x emissions: an overview, *Catal. Sci. Technol.* 7 (2017) 1803–1825.
- [2] D.R. Gentner, S.H. Jathar, T.D. Gordon, R. Bahreini, D.A. Day, I.E. Haddad, P.L. Hayes, S.M. Pieber, S.M. Platt, J. Gouw, A.H. Goldstein, R.A. Harley, J.L. Jimenez, A.S.H. Prévôt, A.L. Robinson, A review of urban secondary organic aerosol formation from gasoline and diesel motor vehicle emissions, *Environ. Sci. Technol.* 51 (2017) 1074–1093.
- [3] B. Frank, M.E. Schuster, R. Schlögl, D.S. Su, Emission of highly activated soot particulate-the other side of the coin with modern diesel engines, *Angew. Chem. Int. Ed.* 52 (2013) 2673–2677.
- [4] P. Granger, V.I. Parvulescu, Catalytic NO_x abatement systems for mobile sources: from three-way to lean burn after-treatment technologies, *Chem. Rev.* 111 (2011) 3155–3207.
- [5] L. Lizarraga, S. Souentie, A. Boreave, C. George, B. D'Anna, P. Vernoux, Effect of diesel oxidation catalysts on the diesel particulate filter regeneration process, *Environ. Sci. Technol.* 45 (2011) 10591–10597.
- [6] D. Fino, S. Bensaid, M. Piumetti, N. Russo, A review on the catalytic combustion of soot in diesel particulate filters for automotive applications: from powder catalysts to structured reactors, *Appl. Catal. A Gen.* 509 (2016) 75–96.
- [7] L.N. Sui, Y.T. Wang, H.Q. Kang, H.Z. Dong, L.F. Dong, L.Y. Yu, Effect of Cs–Ce–Zr catalysts/soot contact conditions on diesel soot oxidation, *ACS Omega* 2 (2017) 6984–6990.
- [8] X. Wang, B.F. Jin, R.X. Feng, W. Liu, D. Weng, X.D. Wu, S. Liu, A robust core-shell silver soot oxidation catalyst driven by Co₃O₄: effect of tandem oxygen delivery and Co₃O₄–CeO₂ synergy, *Appl. Catal. B Environ.* 250 (2019) 132–142.
- [9] T.Z. Liu, Q. Li, Y. Xin, Z.L. Zhang, X.F. Tang, L.R. Zheng, P.X. Gao, Quasi free K cations confined in hollandite-type tunnels for catalytic solid (catalyst)-solid (reactant) oxidation reactions, *Appl. Catal. B Environ.* 232 (2018) 108–116.
- [10] C. Lee, J.I. Park, Y.G. Shul, H. Einaga, Y. Teraoka, Ag supported on electrospun macro-structure CeO₂ fibrous mats for diesel soot oxidation, *Appl. Catal. B Environ.* 174–175 (2015) 185–192.
- [11] A. Stein, F. Li, N.R. Denny, Morphological control in colloidal crystal templating of inverse opals, hierarchical structures, and shaped particles, *Chem. Mater.* 20 (2008) 649–666.
- [12] Y. Wang, H. Arandiyani, J. Scott, A. Bagheri, H.X. Dai, Recent advances in ordered meso/macroporous metal oxides for heterogeneous catalysis: a review, *J. Mater. Chem. A* 5 (2017) 8825–8846.
- [13] V. Alcalde-Santiago, E. Bailón-García, A. Davó-Quinonero, D. Lozano-Castelló, Agustín Bueno-López, Three-dimensionally ordered macroporous PrOx: an improved alternative to ceria catalysts for soot combustion, *Appl. Catal. B Environ.* 248 (2019) 567–572.
- [14] H.L. Wang, B.F. Jin, H.B. Wang, N.N. Ma, W. Liu, D. Weng, X.D. Wu, S. Liu, Study of Ag promoted Fe₂O₃@CeO₂ as superior soot oxidation catalysts: the role of Fe₂O₃ crystal plane and tandem oxygen delivery, *Appl. Catal. B Environ.* 237 (2018) 251–262.
- [15] A. Serve, A. Boreave, B. Cartoixa, K. Pajot, P. Vernoux, Synergy between Ag nanoparticles and yttria-stabilized zirconia for soot oxidation, *Appl. Catal. B Environ.* 242 (2019) 140–149.
- [16] Y.C. Wei, J. Liu, Z. Zhao, Y.S. Chen, C.M. Xu, A.J. Duan, G.Y. Jiang, H. He, Highly Active catalysts of gold nanoparticles supported on three-dimensionally ordered macroporous LaFeO₃ for soot oxidation, *Angew. Chem. Int. Ed.* 50 (2011) 2326–2329.
- [17] J.H. Lee, S.H. Lee, J.W. Choung, C.H. Kim, K.Y. Lee, Ag-incorporated macroporous CeO₂ catalysts for soot oxidation: effects of Ag amount on the generation of active oxygen species, *Appl. Catal. B Environ.* 246 (2019) 356–366.
- [18] Q.Q. Wu, M.Z. Jing, Y.C. Wei, Z. Zhao, X.D. Zhang, J. Xiong, J. Liu, W.Y. Song, J.M. Li, High-efficient catalysts of core-shell structured Pt@transition metal oxides (TMOs) supported on 3DOM-Al₂O₃ for soot oxidation: the effect of strong Pt-TMO interaction, *Appl. Catal. B Environ.* 244 (2019) 628–640.
- [19] C.W. Sun, H. Li, L.Q. Chen, Nanostructured ceria-based materials: synthesis, properties, and applications, *Energy Environ. Sci.* 5 (2012) 8475–8505.
- [20] J.C. Martínez-Munuera, M. Zoccoli, J. Giménez-Mañogil, A. García-García, Lattice oxygen activity in ceria-praseodymia mixed oxides for soot oxidation in catalysed gasoline particle filters, *Appl. Catal. B Environ.* 245 (2019) 706–720.
- [21] D. Jampaiah, V.K. Velisoju, P. Venkataswamy, V.E. Coyle, A. Nafady, B.M. Reddy, S.K. Bhargava, Nanowire morphology of mono- and bidoped α-MnO₂ catalysts for remarkable enhancement in soot oxidation, *ACS Appl. Mater. Interfaces* 9 (2017) 32652–32666.
- [22] F. Ji, Y. Men, J.G. Wang, Y.L. Sun, Z.D. Wang, B. Zhao, X.T. Tao, G.J. Xu, Promoting diesel soot combustion efficiency by tailoring the shapes and crystal facets of nanoscale Mn₂O₄, *Appl. Catal. B Environ.* 242 (2019) 227–237.
- [23] X.T. Lin, S.J. Li, H. He, Z. Wu, J.L. Wu, L.M. Chen, D.Q. Ye, M.L. Fu, Evolution of oxygen vacancies in MnO_x–CeO₂ mixed oxides for soot oxidation, *Appl. Catal. B Environ.* 223 (2018) 91–102.
- [24] X.H. Yu, Z. Zhao, Y.C. Wei, J. Liu, J.M. Li, A.J. Duan, G.Y. Jiang, Synthesis of K-Doped three-dimensionally ordered macroporous Mn_{0.5}Ce_{0.5}O₂ catalysts and their catalytic performances for soot oxidation, *Chin. J. Catal.* 36 (2015) 1957–1967.
- [25] X.H. Yu, Z. Zhao, Y.C. Wei, J. Liu, Ordered micro/macro porous K-OMS-2/SiO₂ nanocatalysts: facile synthesis, low cost and high catalytic activity for diesel soot combustion, *Sci. Rep.* 7 (2017) 43894–43912.
- [26] Q.L. Shi, T.Z. Liu, Q. Li, Y. Xin, X.X. Lu, W.X. Tang, Z.L. Zhang, P.X. Gao, J.A. Anderson, Multiple Strategies to decrease ignition temperature for soot combustion on ultrathin MnO₂-x nanosheet array, *Appl. Catal. B Environ.* 246 (2019) 312–321.
- [27] A.H. Lu, F. Schüth, Nanocasting: a versatile strategy for creating nanostructured porous materials, *Adv. Mater.* 18 (2006) 1793–1805.
- [28] Z. Jiang, Z.X. Zhu, W.Q. Guo, M.X. Chen, W.F. Shangguang, Surface sodium functionalization of ordered mesoporous Co₃O₄ controls the enhanced simultaneous catalytic removal of soot and NO_x, *J. Mater. Chem. A* 5 (2017) 20696–20708.
- [29] H.N. Li, L. Zhang, H.X. Dai, H. He, Facile synthesis and unique physicochemical properties of three-dimensionally ordered macroporous magnesium oxide, gamma-alumina, and ceria–zirconia solid solutions with crystalline mesoporous walls, *Inorg. Chem.* 48 (2009) 4421–4434.
- [30] D. Kuang, T. Brezesinski, B. Smarsly, Hierarchical porous silica materials with a trimodal pore system using surfactant templates, *J. Am. Chem. Soc.* 126 (2004) 10534–10535.
- [31] P.D. Yang, T. Deng, D.Y. Zhao, P.Y. Feng, D. Pine, B.F. Chmelka, G.M. Whitesides, G.D. Stucky, Hierarchically ordered oxides, *Science* 282 (1998) 2244–2246.
- [32] X.H. Yu, L.Y. Wang, Z. Zhao, X.Q. Fan, M.Z. Chen, Y.C. Wei, J. Liu, 3DOM SiO₂-Supported different alkali metals-modified MnO_x catalysts: preparation and catalytic performance for soot combustion, *ChemistrySelect* 2 (2017) 10176–10185.
- [33] J.P. Perdew, K. Burke, M. Ernzerhof, Generalized gradient approximation made simple, *Phys. Rev. Lett.* 77 (1996) 3865.
- [34] Y. Tang, H. Zhang, L. Cui, C. Ouyang, S. Shi, W. Tang, H. Li, J.S. Lee, L. Chen, First-principles Investigation on Redox Properties of M-doped CeO₂ (M = Mn, Pr, Sn, Zr), *Phys. Rev. B* 82 (2010) 125104.
- [35] D.C. Sayle, S.A. Maicananu, G.W. Watson, Atomistic models for CeO₂ (111), (110), and (100) nanoparticles, supported on yttrium-stabilized zirconia, *J. Am. Chem. Soc.* 124 (2002) 11429–11439.
- [36] J. Quiroz, J.M. Giraudon, A. Gervasini, C. Dujardin, C. Lancelot, M. Trentesaux, J.F. Lamorini, Total oxidation of formaldehyde over MnO_x–CeO₂ catalysts: the effect of acid treatment, *ACS Catal.* 5 (2015) 2260–2269.
- [37] X.H. Yu, J.M. Li, Y.C. Wei, Z. Zhao, J. Liu, B.F. Jin, A.J. Duan, G.Y. Jiang, Three-Dimensionally ordered macroporous Mn_{0.5}Ce_{0.5}O₂ and Pt/Mn_{0.5}Ce_{0.5}O₂ catalysts: synthesis and catalytic performance for soot oxidation, *Ind. Eng. Chem. Res.* 53 (2014) 9653–9664.
- [38] Q. Tang, J. Du, B. Xie, Y. Yang, W.C. Yu, C.Y. Tao, Rare earth metal modified three dimensionally ordered macroporous MnO_x–CeO₂ catalyst for diesel soot combustion, *J. Rare Earths* 36 (2018) 64–71.
- [39] T.Y. Gao, J. Chen, W.H. Fang, Q. Cao, W.P. Su, F. Dumeignil, Ru/Mn_xCe_{1-x}O_y catalysts with enhanced oxygen mobility and strong metal-support interaction: exceptional performances in 5-hydroxymethylfurfural base-free aerobic oxidation, *J. Catal.* 368 (2018) 53–68.
- [40] X.M. Zhang, Y.Q. Deng, P.F. Tian, H.H. Shang, J. Xu, Y.F. Han, Dynamic active sites over binary oxide catalysts: in situ/operando spectroscopic study of low-temperature CO oxidation over MnO_x–CeO₂ catalysts, *Appl. Catal. B Environ.* 191 (2016) 179–191.
- [41] T. Taniguchi, T. Watanabe, N. Sugiyama, A.K. Subramani, H. Wagata, N. Matsushita, M. Yoshimura, Identifying defects in ceria-based nanocrystals by UV resonance Raman spectroscopy, *J. Phys. Chem. C* 113 (2009) 19789–19793.
- [42] Z. Wu, M. Li, J. Howe, H.M. Meyer, S.H. Overbury, Probing defect sites on CeO₂ nanocrystals with well-defined surface planes by Raman spectroscopy and O₂ adsorption, *Langmuir* 26 (2010) 16595–16606.
- [43] J.Y. Luo, M. Meng, X. Li, G.X.Y. Q. Zha, T.D. Hu, Y.N. Xie, J. Zhang, Mesoporous Co₃O₄–CeO₂ and Pd/Co₃O₄–CeO₂ catalysts: synthesis, characterization and mechanistic study of their catalytic properties for low-temperature CO oxidation, *J. Catal.* 254 (2008) 310–324.
- [44] M. Ousmane, G. Perrussel, Z. Yan, J.M. Clacens, F. De Campo, M. Pera-Titus, Highly Selective direct amination of primary alcohols over a Pd/K-OMS-2 catalyst, *J. Catal.* 309 (2014) 439–452.
- [45] S.P. Chenakin, G. Melaet, R. Szukiewicz, N. Kruse, XPS study of the surface chemical state of a Pd/(SiO₂ + TiO₂) catalyst after methane oxidation and SO₂ treatment, *J. Catal.* 312 (2014) 1–11.
- [46] M. Mehring, M. Elsener, O. Kröcher, Selective catalytic reduction of NO_x with ammonia over soot, *ACS Catal.* 2 (2012) 1507–1518.
- [47] T. Yamamoto, T. Tanaka, S. Takenaka, S. Yoshida, T. Onari, Y. Takahashi, T. Kosaka, S. Hasegawa, M. Kudo, Structural analysis of iron and manganese species in iron- and manganese-promoted sulfated zirconia, *J. Phys. Chem. B* 103 (1999) 2385–2393.
- [48] S. Liu, X.D. Wu, D. Weng, M. Li, H.R. Lee, Combined promoting effects of platinum and MnO_x–CeO₂ supported on alumina on NO_x-assisted soot oxidation: thermal stability and sulfur resistance, *Chem. Eng. J.* 203 (2012) 25–35.
- [49] M.D. Krcha, A.D. Mayernick, M.J. Janik, Periodic trends of oxygen vacancy formation and C–H bond activation over transition metal-doped CeO₂ (111) surfaces, *J. Catal.* 293 (2012) 103–115.
- [50] H.R. Wu, S.C. Ma, W.Y. Song, E.J.M. Hensen, Density functional theory study of the

- mechanism of formaldehyde oxidation on Mn-doped ceria, *J. Phys. Chem. C* 120 (2016) 13071–13077.
- [51] L. Cheng, Y. Men, J.G. Wang, H. Wang, W. An, Y.Q. Wang, Z.C. Duan, J. Liu, Crystal facet-dependent reactivity of α - Mn_2O_3 microcrystalline catalyst for soot combustion, *Appl. Catal. B: Environ.* 204 (2017) 374–384.
- [52] K. Mori, Y. Iwata, M. Yamamoto, N. Kimura, A. Miyauchi, G. Okamoto, T. Toyoshima, H. Yamashita, An Efficient Cu/BaO/ La_2O_3 catalyst for the simultaneous removal of carbon soot and nitrogen oxides from simulated diesel exhaust, *J. Phys. Chem. C* 118 (2014) 9078–9085.
- [53] H.L. Zhang, C.C. Zhou, M.E. Galvez, P. Da Costa, Y.Q. Chen, MnO_x - CeO_2 mixed oxides as the catalyst for NO-assisted soot oxidation: the key role of NO adsorption/desorption on catalytic activity, *Appl. Surf. Sci.* 462 (2018) 678–684.
- [54] Z.Q. Li, M. Meng, Y.Q. Zha, F.F. Dai, T.D. Hu, Y.N. Xie, J. Zhang, Highly efficient multifunctional dually-substituted perovskite catalysts $\text{La}_{1-x}\text{K}_x\text{Co}_{1-y}\text{Cu}_y\text{O}_{3-\delta}$ used for soot combustion, NO_x storage and simultaneous NO_x -Soot removal, *Appl. Catal. B Environ.* 121–122 (2012) 65–74.
- [55] K. Tikhomirov, O. Krocher, M. Elsener, A. Wokaun, MnO_x - CeO_2 mixed oxides for the low-temperature oxidation of diesel soot, *Appl. Catal. B Environ.* 64 (2006) 72–78.
- [56] X. Guo, M. Meng, F.F. Dai, Q. Li, Z.L. Zhang, Z. Jiang, S. Zhang, Y.Y. Huang, NO_x -assisted soot combustion over dually substituted perovskite catalysts $\text{La}_{1-x}\text{K}_x\text{Co}_{1-y}\text{Pd}_y\text{O}_{3-\delta}$, *Appl. Catal. B: Environ.* 142–143 (2013) 278–289.